Dynamics of Field-Reversed-Configuration in SSX

Abram Falk

Swarthmore College Department of Physics and Astronomy
500 College Avenue, Swarthmore, PA 19081

afalk1@swarthmore.edu

March 22, 2003

Abstract

The Field Reversed Configuration (FRC) is a novel high β magnetic confinement scheme, which has not been as extensively investigated compared to other schemes like the tokomak. The Swarthmore Spheromak Experiment (SSX) forms hybrid spheromak/FRCs using the merging spheromak technique. A soft x-ray detector and a Mach probe are valuable diagnostics, especially for measuring the various forms of energy that are released when the two spheromaks merge in a magnetic reconnection process. By comparing the soft x-ray detector data to simulated emission spectra, electron temperature can be inferred. This analysis yields $T_e = 30 \pm 10$ eV for SSX, where the large uncertainty reflects the uncertainty in the impurity content of SSX. There is found to be more heating, apparently due to more reconnection, when the merging spheromaks are of counter-helicity rather than when they are co-helicity. The Mach probe has measured azimuthal ion velocity, which is probably caused by the $\mathbf{J} \times \mathbf{B}$ force.

Contents

Chapter 1

Introduction

Simultaneously responding and contributing to the electromagnetic field, charged particles in a plasma are dynamically entangled with the field. In tracing these entanglements, plasma science loses the innocence of closed-form exact solutions and the simplicity of separating action from reaction. However, what is lost in simplicity is gained in richness. The complexity of the particle-field coupling leads to a state of matter that supports an impressive capacity for global structure.

Even if plasma dynamics were not interesting, we could not ignore the plasma state of matter because, although rare on earth, it constitutes the bulk of the universe. Due to the disparity between the small amount of plasma we directly experience and the large amount that exists in space, many basic astrophysical processes are not understood.

One of these problematic processes is coronal heating. At a temperature of 5400 K, the surface of the sun is hot indeed. Even hotter, however, is the coronal region, just beyond the surface. This region can reach temperatures greater than 1,000,000 K, according to emission spectroscopy. Normal thermodynamic processes do not explain this heating–it would be like the air above the 300 K ocean being 60,000 K. What does explain it then? One hypothesis is that the heating is caused by magnetic reconnection, a process in which two oppositely oriented magnetic fields come into contact, as shown in figure 1.1. The topology of the field lines changes at this event, and the opposing field lines annihilate. The energy that was once stored in the magnetic fields is converted into other forms of energy, one of which is heat.

The new field of physics that has emerged to test astrophysical hypotheses like this one is called laboratory astrophysics. Astrophysicists seek to understand plasma energetics and dynamics in the universe, by replicating these processes in the laboratory. The driving notion is that experiments can be *well-scaled*, where size notwithstanding, certain dimensionless parameters can be the same in the laboratory as they are in space. With these dimensionless parameters held constant, the necessarily smaller scale of the laboratory ought not to shroud the fundamental physical processes. In the laboratory, the plasma can be probed and controlled in ways that would be impossible in a solar-scale plasma. One of these laboratory astrophysical experiments is the Swarthmore Spheromak Experiment (SSX), which was developed to replicate the magnetic reconnection processes that are supposed to occur in the solar corona.

As laboratory astrophysics experiments seek a fundamental understanding of astronomical processes, a different breed of plasma experiments is after something different: power. These experiments comprise the fusion program, and their objective is essentially to build a miniature star on earth, to make fusion a viable energy source. The challenge for fusion scientists is confinement–it is pretty easy to make a fusion bomb, but much harder to confine the fusion reaction into a regulated reactor. Since fusion reactions require a plasma with a minimum temperature of about 100 million K, the reaction cannot be confined by physical walls. The most successful approach has been Magnetically Confined Fusion, whereby the plasma containing the reactants is confined in a magnetic bottle. This bottle, of course, needs to be generated by an electrical current either inside or outside the plasma, and various types of bottles have been tried. The Swarthmore Spheromak Experiment is investigating a novel confinement scheme called Field-Reversed Configuration (FRC), in which the confining magnetic field is sustained not externally but by the plasma itself.

Although plasma in the laboratory is much easier to observe than astrophysical plasma, to extract information from it can still be a challenge. A plasma has many important qualities and quantities, such as magnetic field, temperature, density, ion flow, and current flow, but there is no single omniscient diagnostic. Since magnetic reconnection is a magnetic event and FRC is a magnetic confinement scheme, the magnetic probe array on SSX is a chief diagnostic. This thesis will focus on two other complementary diagnostics, namely the soft x-ray (SXR) detector and the Mach probe, both of which I designed and built for SSX. Those who are unfamiliar with plasma physics might prefer to read chapter 3 first.

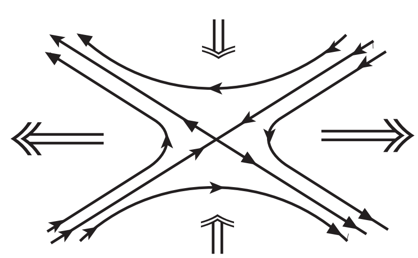

Figure 1.1: Magnetic reconnection. The large arrows represent the direction of flow and the directed curves are magnetic field lines. Two opposing magnetic fields flow into each other and the fields are annihilated. The magnetic energy is released in a reconnection outflow (left and right in this diagram) and heat. This process is explained in detail in chapter 3.3.

Chapter 2

Toward a Magnetically Confined Fusion Reactor

The development of controlled nuclear fusion has a rich interaction with basic plasma science. The ambition of achieving an inexhaustible fuel source has prompted much of the basic plasma research in the twentieth century. Conversely, advances in the science of controlled fusion have frequently been the products of advances in the understanding of fundamental plasma processes.

Two light nuclei can fuse together to form a heavier nucleus and a free energetic nucleon. This process is the core physical reaction of the fusion reactor. Since fusion is a nuclear reaction, large amounts of energy are released, MeVs per reaction. The catch is that, since nuclear forces are short-range, the incoming nuclei must have large kinetic energies, at least 20 keV to overcome the Coulomb repulsion between the two positively charged nuclei. This means that in order to have a significant reaction rate, the reactants must be very hot, at least 10 keV (100 million K). A steady state reactor requires a temperature of about 30 keV (350 million K). At these temperatures, matter is a very hot plasma. This is the basis of the collusion between fusion energy science and plasma science.

2.1 Confinement

The requisite 10 keV engenders the very difficult containment problem: in what bottle should this very hot plasma be stored? A solid container is not practical, because the contact between the container and the plasma would cool the plasma and damage the container. There are three practical approaches.

1. Gravitational Confinement Fusion

A strong gravitational well is the most effective confinement scheme, as all matter is pulled to its center. This is the method of the sun and stars. However, since the gravitational force is so weak, in order to trap fast particles the gravitational well must be generated by an extraordinary quantity of mass. In other words, only stars can use this method.

2. Inertial Confinement Fusion (ICF)

A small container called a "hohlraum" can be imploded by a laser, heating and compressing a fuel pellet within. If the hohlraum is imploded very symmetrically, fusion reactions can occur in the plasma before the constituent materials explode. If such a device were large scale and used a fission explosion instead of lasers for the implosion, it would be a hydrogen bomb. The major challenge for ICF is the implosion symmetry must be so great that over two-hundred very large lasers must be used, and even the theoretical Q (defined to be the ratio of output power to consumed power) is not much over 1.

3. Magnet Confinement Fusion (MCF)

MCF is the most developed of the three types of containment, and the only type that we will deal with in this thesis. The essence of MCF is to exploit the fact that a plasma is composed of charged particles and can hence be held in a "magnetic bottle," if the "bottle" design is clever enough not to have many leaks. By a mathematical theorem, there is no purely electrostatic container for a plasma that is stable.

Magnetically confined plasmas have several important parameters. There are separate ion and electron temperatures, $\mathrm{T_i}$ and $\mathrm{T_e}$ respectively, as the two species often do not equilibrate. In this thesis, we will not be careful to distinguish the two temperatures. The confinement time τ measures how long the magnetic "bottle" will stay intact before turbulence or other transport transport processes rip it apart. The kinetic pressure is the product of the density n and T, and the magnetic energy density $\frac{B^2}{2\mu_0}$ can be thought of as a confining pressure. The ratio of kinetic pressure to magnetic pressure is called β. Though β must be less than 1 for a confined plasma, a high β helps a plasma reach higher temperatures, since often the magnetic field is limited by the strength of the physical materials. The triple product $n\mathrm{T}\tau$ is a good measure of how much fusion power is produced.

2.2 Fusion Reactions

There are several different fusion reactions that could be used in a fusion reactor, most having the deuterium and tritium isotopes of hydrogen as reactants. The ones of interest are [2]:

$$\mathrm{p} + \mathrm{p} \longrightarrow \mathrm{D} + \mathrm{e}^+ + \text{neutrino} + 1.4\ \mathrm{MeV} \tag{2.1}$$

$$\mathrm{D} + \mathrm{T} \longrightarrow \mathrm{He}^4\ (3.5\ \mathrm{MeV}) + \mathrm{n}\ (14.1\ \mathrm{MeV}) \tag{2.2}$$

$$\mathrm{D} + \mathrm{D} \longrightarrow \mathrm{T}\ (1.0\ \mathrm{MeV}) + \mathrm{p}\ (3.0\ \mathrm{MeV}) \tag{2.3}$$

$$\mathrm{D} + \mathrm{D} \longrightarrow \mathrm{He}^3\ (0.8\ \mathrm{MeV}) + \mathrm{n}\ (2.5\ \mathrm{MeV}) \tag{2.4}$$

$$\mathrm{D} + \mathrm{He}^3 \longrightarrow \mathrm{He}^4 (3.7\mathrm{MeV}) + \mathrm{p}\ (14.7\ \mathrm{MeV}) \tag{2.5}$$

Additionally, a combination of reactions 2.2 and 2.3 is a good candidate for a reactor. In order for a fusion reaction to generate a significant amount of energy, it must have a large reaction rate, defined to be $\langle \sigma v \rangle$, where σ is the cross-section of the reaction and $<>$ indicates an average over velocities. It is important to remember that the temperature of a plasma indicates not the speed of all the particles in the plasma, but the distribution of velocities, which in thermal equilibrium will be a Gaussian. Thus the reaction rate is nonzero (although possibly negligible) for all temperatures, but it is a strong function of temperature. This is what allows us to speak of a "minimum" temperature needed for a fusion reaction.

The various fusion reactions are suitable for different devices. Reaction 2.1 is the primary fusion reaction on the sun, but its cross-section is far too small to be suitable for any devices on earth. Reaction 2.2 is what the first engineered fusion devices have used, since it has the largest cross-section by far. It has the disadvantage of requiring tritium as a reactant. Since tritium is radioactive, an extra class of concerns are necessary to consider when designing a D-T reactor. Reaction 2.3 has a smaller cross-section than 2.2, but it does not require tritium as a reactant. The tritium that is a product of this reaction can then be burned in a D-T reaction. Reaction 2.4 has a smaller cross-section still, but has the advantage that it involves no radioactive element as either a reactant or a product. Reaction 2.5 is an alternate non-radioactive fusion reaction, with a larger cross-section than 2.3 or 2.4. Reaction 2.5 is especially suited for confinement schemes with high β, such as Field-Reversed Configuration. Although He^3 is not found on the earth, it could be obtained from the lunar surface, which contains a few parts per billion He^3 due to the solar wind.

2.3 Torus Topology

The basic idea behind magnetic confinement is very easy if we grossly simplify the physics. Magnetic field lines are approximately guiding-center trajectories for particles in a plasma. This fact is plausible from the Lorentz force law (equation 3.3) which, if the fields are constant, directly predicts that particles will orbit magnetic field lines. In this picture, the particles' freedom of motion has been confined in two out of three dimensions, although it can still move freely along the magnetic field line about which it is circling. Closing the field line, as shown in figure 2.1, confines the particle in the last dimension. As discussed below, some important physics are left out here. Nevertheles, this shows why the torus, a.k.a. the dougnut, is the natural shape for a fusion reactor.

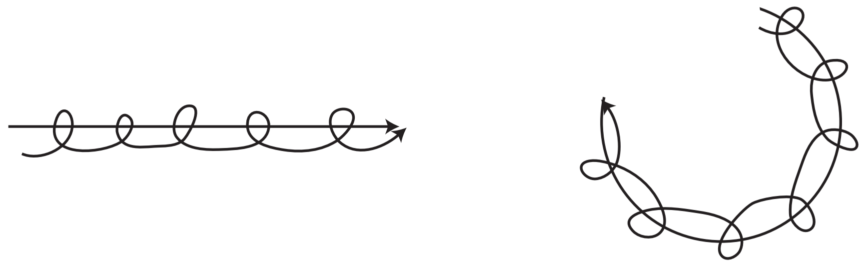

Figure 2.1: *Left:* an ion is confined to a magnetic field line. The radius of the helices in which it is travelling is the Larmor radius r_L. *Right:* To confine the particle in the remaining dimension, the confining field line is chosen to be closed.

A dougnut is a compact surface of genus 1, since it has 1 hole. One might wonder if it is possible to confine particles within a compact surface of genus 0, that is, to within a dougnut-hole. After all, a furnace can reach higher temperatures with a smaller surface area to volume ratio, and surfaces of genus 0 tend to have the smallest surface area. It is a basic topological fact that this confinement scheme is not possible. In order to confine a particle to a torus, we would need to cover the surface of the torus with a magnetic field that is everywhere tangent to the torus. If we think of the magnetic field as an abstract vector field, this is equivalent to covering a dougnut with sprinkles of various lengths such that the sprinkles join tip-to-tail. Furthermore, since magnetic fields are always continuous, the tangent field covering the torus has to be continuous. However, a mathematical theorem says that any continuous vector field tangent to a compact surface of genus 0 has at least two degenerate points, which is to say two points where the sprinkle size is zero. At these points, there would be no confining magnetic field, and particles would escape. Hence a surface topologically equivalent (diffeomorphic) to a sphere could never magnetically confine a plasma.

This is why the magnetic topology of confinement schemes are of genus 1. Note that this argument outrules schemes with genus 0 magnetic topology, but leaves open the possibility of a genus 1 magnetic structure framed in a physical container of genus 0. We will see that this possibility is very real.

2.4 The Tokamak

Unfortunately, the simple picture of closed magnetic field lines forming a torus, about which ions and electrons circle, leaves out some important physics. When a magnetic field line is bent, other forces arise, which act on the particle's guiding centers, namely curvature drifts and $\nabla\mathbf{B}$ drifts. A successful confinement scheme must find a way to neutralize these other forces and stabilize the confinement.

The tokamak is the most developed among these schemes. The tokamak concept stabilizes the confinement by having the magnetic topology be comprised of both *toroidal* and *poloidal* fields. *Toroidal* refers to directions traced out by circles on a dougnut enclosing the dougnut-hole, whose axis is the axis of the torus. *Poloidal* fields, on the other hand, pass through the dougnut-hole. The sum of these two fields are magnetic field lines that circle in both directions, that toroidally orbit the dougnut-hole but also "twist." The helical motion of the particles causes the curvature drifts to be neutralized.

An axisymmetric geometry implies that toroidal fields are generated by poloidal currents and vice-versa. In a tokamak, electric currents in poloidal coils outside the plasma produce the toroidal field, typically 5-10 T [2]. The poloidal fields are harder to produce because the current that generates them must be inside the plasma. A current (typically 15-25 MA [2]) can be induced in the plasma by a steadily increasing current in an external solenoidal coil, effectively making the plasma the secondary in a transformer current. The external solenoid is located in the hole of the dougnut.

Since plasma is slightly resistive, the induced toroidal current also heats the plasma. This is called ohmic heating. However, since in plasma, $\rho \propto T^{-\frac{3}{2}}$, ohmic heating is negligible above 2-3 keV. Above this, auxiliary heating methods are necessary, if a plasma is to reach the 10-30 keV required for fusion. These methods include the injection of energetic ions, rf-waves, and heating by fusion itself, if the reaction rate is large enough.

A persistent problem in the development of controlled fusion and the tokamak in particular has been turbulence. No confinement scheme can be perfect, as Coulomb collisions will always lead to diffusivity. Fortunately, the effects of diffusive transport are relatively benign. For many years, magnetic confinement experiments suffered from the so-called "anomalous transport" problem, in which observed transport exceeded theoretically predicted transport by one or two orders of magnitude. This discrepancy turned out to be due to turbulence, large scale instabilities in the plasma. A key task for fusion science researchers is to find ways to tame these instabilities.

The Russian physicists Tamm and Sakharov invented the tokamak concept in 1950. Tokamak is a Russian acronym for "toroidalnaya kamera i magnitnaya katushka," or "toroidal chamber and magnetic coil." After the successful Russian T-3 experiment in the 1960's, the tokamak was embraced by the US, Europe, and Japan, and the tokamak was scaled up and optimized. Tokamak progress has been steady ever since. The two largest tokamaks, TFTR at Princeton and the Joint European Torus in the UK, have approached the break-even condition $Q = 1$. ITER, latin for 'the way', will be an international effort at a tokamak that is hot enough to reach 'ignition,' the point at which the fusion reactions in a plasma can heat the plasma instead of auxiliary methods. Construction for ITER begins in 2004. A commercially viable reactor prototype is forecasted to be built by 2030.

Nevertheless, in the early '90's the fusion science community decided that confinement configurations besides the tokamak should be explored. Since it appeared that a commercially viable reactor was still many years down the road, there was still time for basic plasma research to make contributions. Furthermore, whereas the β parameter for a tokamak is stuck at 5-10 %, β for some of the alternate schemes approaches 100%, making them a practical choice for 'advanced' fusion reactions (i.e. reactions not the D-T reaction).

2.5 The Spheromak

To stabilize the tokamak with a poloidal magnetic field that is sustained from a current inside the device is to exploit one of the most useful properties of plasma: that the same charges which respond to the electromagnetic field also create a field of their own. A logical extension of this idea is to try to form a confining magnetic bottle that is sustained entirely from currents in the plasma, a sort of equilibrium between plasma charges and field. Of course, the tokamak could never be one of these equilibrium configurations, since its basic toroidal field is generated by external poloidal coils. In fact, even the toroidal current in a tokamak requires a hefty external current drive through the center of the device.

However, such equilibrium configurations do exist. Among these, one of the most famous is the spheromak. Like the tokamak, the spheromak's magnetic structure is a torus. Also like the tokamak, the spheromak is a low-β configuration ($\beta \approx 10\%$). Unlike the tokamak, however, a spheromak relaxes to equilibrium within a simple container, not a toroidal one. Hence a spheromak is a member of the compact toroidal equilibrium family. It is shown below in figure 2.2.

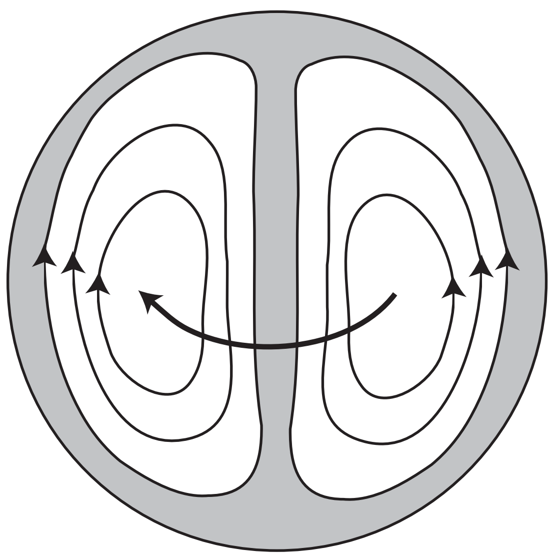

Figure 2.2: A cross-section of the spheromak. The field lines in the page of the page are poloidal, and the field lines which cut through the page are toroidal.

A spheromak can be described by ideal magnetohydrodynamics (MHD). Discussed in Chapter 3.1, ideal MHD is a simple set of fluid equations describing plasma. The spheromak is a series of solutions to the Grad-Shafranov equation, which is an differential equation that describes axisymmetric plasma equilibria in the MHD limit.

As discussed in (Chapter 3.2), in the ideal MHD limit, magnetic flux is “frozen” into the plasma fluid. This means that in a spheromak, poloidal and toroidal magnetic fields sustain each other. Toroidal (resp. poloidal) magnetic fields are frozen into toroidal (poloidal) currents, which generate poloidal (toroidal) fields.

2.5.1 A Force-Free State

Let us explore the sort of equilibrium that describes a spheromak. Azimuthally-symmetric plasma equilibria that can be analyzed in the MHD framework are in general called Grad-Shafranov equilibria. However, the low-β spheromak satisfies an even stronger equilibrium condition.

A key notion to understanding the spheromak is *helicity*, defined to be

$$K = \int \mathbf{A} \cdot \mathbf{B} \mathrm{d}^3 r. \tag{2.6}$$

Roughly speaking, the helicity of a spheromak describes how the toroidal and poloidal magnetic fluxes are linked–if you keep the poloidal flux the same and reverse the toroidal flux, the sign of K reverses. The reason helicity is an important concept is that it is a conserved quantity in both microscopic instabilities and magnetic reconnection [4]. The equilibrium condition can be derived by minimizing the total magnetic energy $W = \int \mathrm{d}^3 r B^2/2\mu_0$ subject to the constraint that helicity is conserved. Note that it is acceptable to minimize W instead of the total energy $W + nkT$, because the spheromak is a low β configuration, so $nkT \ll W$. The Lagrange multiplier solution to this variational problem is [4]

$$\delta W - \lambda \delta K = 0 \tag{2.7}$$

$$\implies \int \mathbf{B} \cdot \delta \mathbf{B} \mathrm{d}^3 r - \lambda \int (\mathbf{A} \cdot \delta \mathbf{B} + \mathbf{B} \cdot \delta \mathbf{A}) = 0 \tag{2.8}$$

$$\implies \int \mathbf{B} \cdot \nabla \times \delta \mathbf{A} \mathrm{d}^3 r - \lambda \int (\mathbf{A} \cdot \nabla \times \delta \mathbf{A} + \mathbf{B} \cdot \delta \mathbf{A}) = 0, \tag{2.9}$$

using $\delta \mathbf{B} = \nabla \times \delta \mathbf{A}$. Now we can use integration by parts on equation (2.9). If we assume that $\mathbf{B} \cdot \mathrm{d}\mathbf{s} = 0$ on the surface of the spheromak (magnetic flux does not poke out), then we have

$$\int (\delta \mathbf{A} \cdot \nabla \times \mathbf{B}) \mathrm{d}^3 r - \lambda \int \mathbf{B} \cdot \delta \mathbf{A} \mathrm{d}^3 r = 0, \tag{2.10}$$

or

$$\int (\nabla \times \mathbf{B} - \lambda \mathbf{B}) \delta \mathbf{A} \mathrm{d}^3 r = 0. \tag{2.11}$$

The integrand must vanish since $\delta \mathbf{A}$ is arbitrary. Thus we have the condition

$$\nabla \times \mathbf{B} = \lambda \mathbf{B}. \tag{2.12}$$

Magnetic field structures that obey this equation are called Taylor states. An important property of Taylor equilibria is manifest if we use Ampere's Law to rewrite the equilibrium condition (equation 2.12) as

$$\mu_0 \mathbf{J} = \lambda \mathbf{B}. \tag{2.13}$$

What this equation implies is that $\mathbf{J} \times \mathbf{B} = 0$, which is the definition of a *force-free* equilibrium configuration. Looking at equation (3.6), we see why the term *force-free* is used: if the configuration is steady-state and there is no pressure, then the force-equation for a conducting fluid reduces to $\mathbf{J} \times \mathbf{B} = 0$. The parameter λ has units $length^{-1}$ and functions as an eigenvalue.

2.5.2 Spheromak Formation

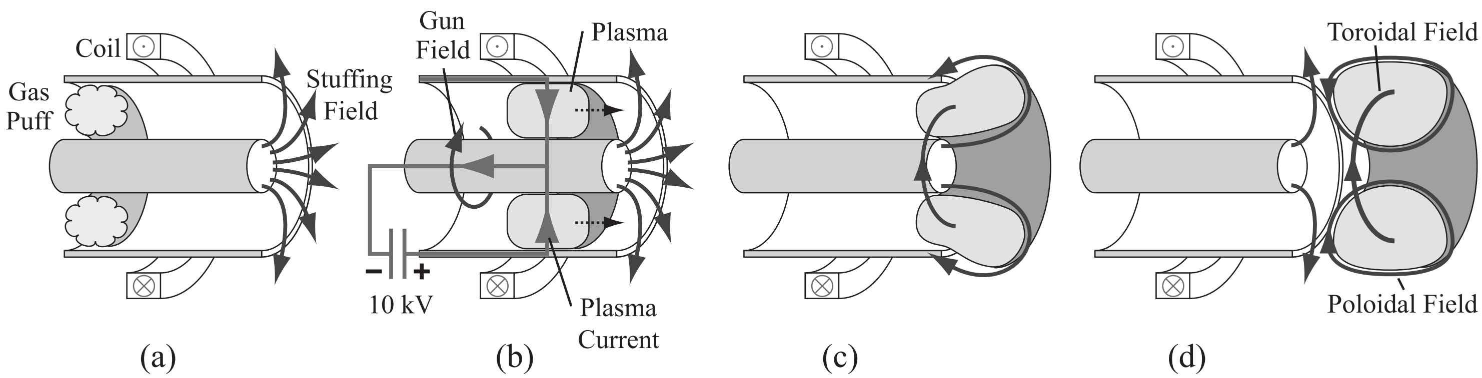

Figure 2.3: Spheromak formation

In SSX, two spheromaks are formed simultaneously, on either side of the device. A common way of forming spheromaks, which is the way they are generated in SSX, is with a magnetized coaxial gun. This process is illustrated in figure (2.3). In figure (2.3a), a coil outside the gun generates a magnetic field in the chamber called the stuffing field. The cylindrical object in the chamber is the center electrode, which consists of a conductive copper shell surrounding a highly permeable material.

After the stuffing field has soaked through the flux conserver, a puff of pure hydrogen gas is allowed to fill the gun chamber. In figure (2.3b), the capacitor banks fire, and the gun receives a large negative potential. The hydrogen gas is ionized, a a large inward-pointing $\mathbf{E}$ field arises, driving an inward-pointing $\mathbf{J}$. Furthermore, as a large current flows leftwards through the gun, this current also generates an azimuthal $\mathbf{B}$ field in the gun chamber. Using equation (3.6), we see that $\mathbf{J} \times \mathbf{B}$ is a force. Since in this situation, $\mathbf{J}$ is radial and $\mathbf{B}$ is azimuthal, $\mathbf{J} \times \mathbf{B}$ is axial, and the plasma is pushed out of the gun, distending the stuffing field (figure (2.3c). The poloidal magnetic field is inherited from the stuffing field. Finally, in figure (2.3d), the spheromak breaks away from the coaxial gun. The handedness of the spheromak refers to the handedness of the toroidal field with respect to the poloidal field.

2.6 Field Reversed Configuration

Like the spheromak, the Field Reversed Configuration (FRC) [10] is a compact toroidal equilibrium state. The topological difference between a spheromak and an FRC is that whereas a spheromak has a strong toroidal magnetic field, an ideal FRC has no such toroidal field–the magnetic field of an ideal FRC is entirely poloidal.

The Field Reversed Configuration is a potentially advantageous containment scheme. Because field-reversed configuration has a near unity β, it is suitable for achieving the high temperatures necessary for advanced fusion reactions, like the $\mathrm{D}-\mathrm{He}^3$ (equation 2.5) reaction.

However, the FRC is only a suitable confinement scheme if it is stable in the MHD regime (see chapter 3.1 about MHD). Diffusion makes any confinement scheme imperfect, but MHD instabilities can be prohibitively deleterious, threatening the global magnetic structure. Of course, in plasma physics, stability cannot be thought of in black-and-white terms, like a ball either on a hill or in a valley, as the terrain has far too many dimensions. Hence the stability question is one of degree.

One way to observe FRC stability is to observe FRC *modes*. Like the spheromak, the FRC is a Grad-Shafranov equilibrium state, and there are a series of FRC modes which solve the differential equilibrium equation. The $m = 0$ mode is the basic FRC mode, which is potentially stable. The $m = 1$ mode is called the tilt mode, and an unstable $m = 0$ FRC can "roll over" into this tilt mode if it is unstable. Whether the plasma configuration in SSX-FRC is an $m = 0$ FRC or a $m = 1$ tilted FRC can be observed using the magnetic probes.

Field Reversed Configuration has an outstanding discrepancy between theory and experiment. MHD and kinetic simulations predict that FRCs should be very unstable to the tilt mode (see diagram in final draft) [13]. However, actual experimental FRCs are anomalously resistant to this instability [11] [12]. There must be a stabilizing mechanism in an experimental FRC that was not included in these simulations.

Recent calculations [14] [15] from a hybrid model (fluid electrons, particle ions) have found that this stabilizing mechanism might be equal and opposite toroidal magnetic fields or ion velocities that emanated spontaneously in a simulated FRC. One of the purposes of SSX-FRC is to see what sort of stabilizing effect the addition of a toroidal field has on an FRC.

2.6.1 Merging Spheromak Technique for FRC Formation in SSX

The merging spheromak technique for FRC formation was invented at the the TS-3 device at the University of Tokyo [6]. Two spheromaks are formed on either end of the device, with opposing helicities, so that the two spheromaks have both opposing toroidal and poloidal magnetic fields. A schematic of is shown is shown in figure 2.4. Traveling towards each other at the Alfvèn speed, they intersect at the midplane, at which point magnetic reconnection occurs. They found that the opposing toroidal magnetic flux is essentially annihilated entirely if the two initial spheromaks are equal in magnitude. However, the poloidal flux is only partially annihilated. The reconnected poloidal flux that is not annihilated forms an FRC. This is called the merging technique for FRC formation.

At SSX-FRC, we actually do not find that the opposing toroidal flux annihilates [44]. An FRC with residual toroidal flux is called a hybrid FRC [9] state.

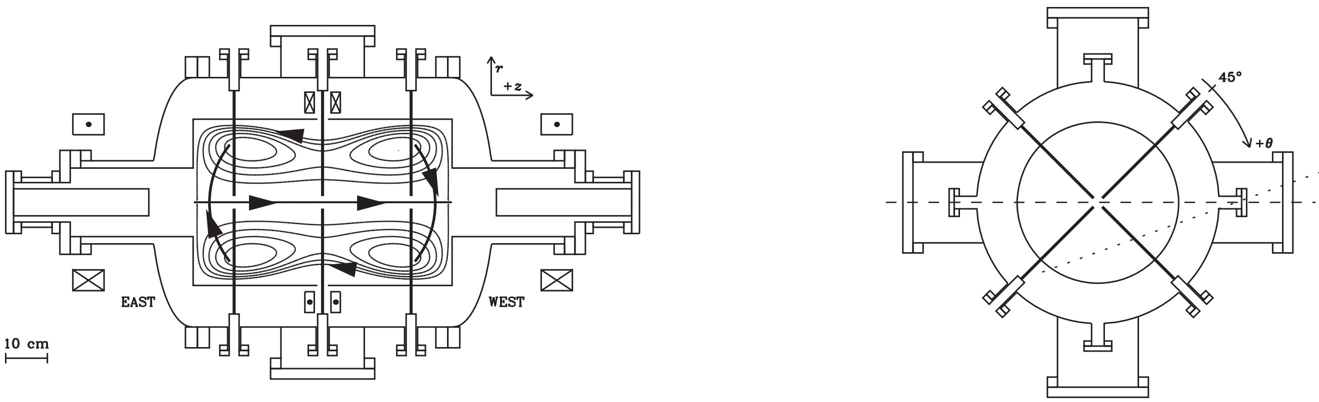

Figure 2.4: *Left:* A side view of an FRC structure in SSX. Actually, this is a hybrid FRC. If it were a pure FRC, there would be no toroidal (azimuthal) field. *Right:* An end view of SSX. The slanted dashed line is the initial line of sight of the SXR detector, though in the data presented in this thesis, it is looking straight through the midplane.

The usual technique for FRC formation is the field-reversed theta-pinch method, in which a strong azimuthal current is turned on and then sharply reversed. As the axial magnetic field reverses, the magnetic field lines connect to form an FRC. A weakness of the theta-pinch method is that it produces small amounts of magnetic flux, not more than tens of mWb [16]. It also typically produces plasmas with small s, where s is approximately the number of ion gyroradii in the minor radius of the device. A reactor-grade plasma will need to have Webers of magnetic flux [16] and large s. The merging spheromak technique allows the large s region to be explored.

Since the two spheromaks start out with opposite helicity, and helicity is conserved, the resulting FRC has helicity 0. On the other hand, if we set the device so that the helicities of the two spheromaks are the same, then instead of partially annihilating each other, the two spheromaks relax into one larger spheromak [8].

2.7 Swarthmore Spheromak eXperiment: the Device

The Swarthmore Spheromak Experiment is an eight year old device, originally built to study the magnetic reconnection of two spheromaks. In the past year, it has been modified to observe FRC stability using the merging spheromak technique. The new experiment is called SSX-FRC (though we still call it SSX for short).

The SSX vacuum tank is a stainless steel right cylinder 0.60 m in diameter, with ports for diagnosis on three axial planes, designated east, midplane, and west. The vacuum pump is an oil-free cryogenic system, which maintains a pressure of about 2×10^{-7} torr. It has two identical spheromak sources, which generate spheromaks by the method discussed in chapter 2.5.2. The two guns are powered by two high voltage (10 kV) pulsed power supplies. Within the steel vacuum tank is a 0.4 m copper flux conserver, which is the vessel in which the plasma is contained.

A typical SSX-FRC plasma has 3-4 mWb poloidal flux, 1 kG edge field, 1 $\times 10^{15}$ cm^{-3} density, 30 eV temperature, and $s > 10$ [8].

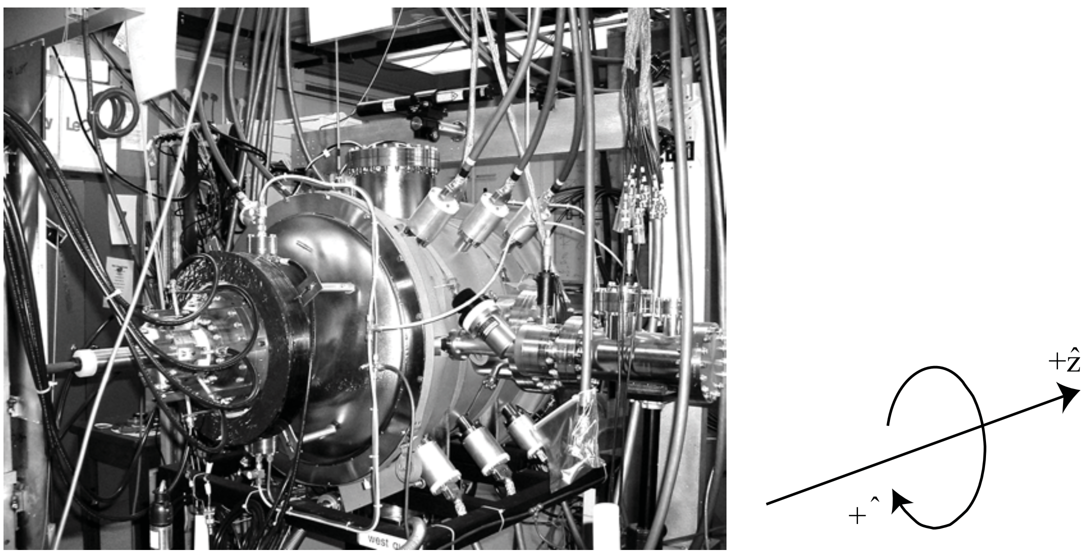

Figure 2.5: A photo of the SSX vacuum chamber with its many diagnostics. A cylindrical coordinate system puts the z-axis along the axis of the cylindrical chamber and theta as the toroidal coordinate.

In addition to the soft X-ray detector and the Mach probe, diagnostics on SSX include a He-Ne (633 nm) interferometer, which measures line averaged density; a bolometer, which measures total radiated power; a vacuum ultraviolet spectrometer; and the several magnetic probe arrays (600 coils). The vacuum ultraviolet spectrometer differs from the SXR detector in that its spectrum is softer and its bandwidth, while adjustable, is much narrower. A screen room protects the data collection electronics from electromagnetic noise.

A novel piece of hardware that SSX-FRC has is a Reconnection Control Coil (RCC), which is a toroidal coil in the vacuum chamber. This coil provides an axial magnetic field of up to 700 G (on axis). Its purpose is to inhibit magnetic reconnection. By increasing the RCC field, one can control the reconnection and investigate the stability of a non-ideal FRC with a residual toroidal field.

Chapter 3

Some Basic Results from Plasma Physics

Plasma is frequent called the fourth state of matter, after solid, liquid, and gas. Though the latter three are more familiar on earth, plasma constitutes an estimated 99 % of matter in the universe. The qualitative properties of solids, liquids, and gases are familiar to everyone. Plasma, too, has qualitative characteristics, beyond that it is an ionized gas, which is a microscopic trait and, furthermore, a quantitative trait, since all gases are ionized to some small degree. A good qualitative description of plasma is "a quasineutral gas of charged and neutral particles which exhibits collective behavior" [1].

The quasineutrality of plasma occurs not despite the fact that plasma is composed of charged particles, but because of it. What quasineutrality refers to is Debye shielding. If you wanted to insert an electric field into an unionized gas, all you would have to do is insert a charge into the gas, and Coulomb's law would imply an electric field that permeates it. However, if you were to insert a charge, say of value +q, into a plasma, electrons would flock about the charge, and their field would shield out the charge's field in the limit of being far from the charge. Actually, the distance greater than which the charge is shielded is not that far. Poisson's equation and the electron distribution function imply that this distance, called the Debye length, is

$$\lambda_D = \sqrt{\frac{\epsilon_0 K T_e}{n e^2}} \tag{3.1}$$

The sphere of radius λ_D about the charge is known as the Debye sheath. Within the sheath, the field of the inserted charge can be felt, and outside of it, the field is shielded. Thus quasineutrality means that local charge or electric field will be shielded. A plasma is called quasineutral if its characteristic dimension is much greater than the Debye length:

$$Ł \gg \lambda_D. \tag{3.2}$$

Plasma's other principle quality is its ability to exhibit collective behavior. Whereas particles of an unionized gas interact only collisionally, which is not conducive for global structure, charged particles can interact in a plasma with the long range electric and magnetic forces. The Debye mechanism shields plasma from a local static perturbation of charge or potential, but dynamic effects and global structure are not defeated. This is what makes plasma physics a rich field.

3.1 The MHD approximation

The basic equation of motion for particles in a plasma is simply the Lorentz force law

$$\mathbf{F} = q(\mathbf{E} + \mathbf{v} \times \mathbf{B}), \tag{3.3}$$

along with Maxwell's equations, which specify the evolution of the E and B fields from the charged particles' positions and velocities. The density of SSX, a fairly typical plasma, is about $10^{15}\mathrm{cm}^{-3}$. This means that to solve the equations of motion for even a cubic centimeter of plasma one has to solve 10^{15} second-order coupled differential equations, an unpleasant task at the very least! Moreover the solution to this giant system of equations does not automatically lead to understanding of the qualitative behavior of the plasma.

The resolution of this problem is to contract the mathematical representation of the plasma into the simpler model of a conducting fluid. Actually, there will be two conducting fluids, one for the electrons and one for the ions. However, it is possible to further contract this two-fluid model into a one-fluid model called MHD. In a fluid model, the state of the system is described not by the position and velocities of individual particles, but rather by only a few variables, namely density ρ, pressure p, and flow velocity $\mathbf{V}$, which can be functions of space.

In a non-conducting fluid, fluid elements experience a force solely because of pressure gradients. Newton's law gives the force equation:

$$\rho \frac{\mathrm{d}\mathbf{V}}{\mathrm{d}t} = -\nabla p \tag{3.4}$$

The derivative in this case is the convective derivative

$$\frac{\mathrm{d}}{\mathrm{d}t} = \frac{\partial}{\partial t} + \mathbf{V} \cdot \nabla \tag{3.5}$$

The first term of the convective derivative is the explicit time dependence and the second term accounts for the effect of flow. A good analogy for the convective derivative is if you are swimming in a lake and measuring the temperature of water as you swim with velocity $\mathbf{V}$. The total variation in temperature that you experience can come from either the temperature of the water changing at each point (the $\frac{\partial}{\partial t}$ term) or from the fact that your movement through a temperature-varying lake causes you to feel hotter or colder, even if the lake's temperature is time-independent (the $\mathbf{V} \cdot \nabla$ term).

A conducting fluid model is described by these variables plus the current density $\mathbf{J}$ variable. In the conducting fluid approximation, the force on a fluid element can either be from pressure gradients or from the Lorentz force:

$$\rho \frac{\mathrm{d}\mathbf{V}}{\mathbf{d}t} = -\nabla p + \mathbf{J} \times \mathbf{B} \tag{3.6}$$

This is the first MHD equation. The second is the continuity equation, which says that mass is locally conserved. In other words, the change in density at a point must be because there is a flow of mass either into or out of that point:

$$\frac{\partial \rho}{\partial t} = -\nabla \cdot (\rho \mathbf{V}) \tag{3.7}$$

The third MHD equation is that the pressure of the equation of state for the plasma:

$$p\rho^{-\gamma} = \text{constant}, \tag{3.8}$$

where γ is the ratio of heat capacities. $\gamma = 1$ in an isothermal system and $\frac{n+2}{n}$ in an adiabatic system, where n is the number of degrees of freedom. In an adiabatic hydrogen plasma, $\gamma = 5/3$.

The fourth MHD equation is the force-balance equation. It expresses the coupling of the plasma to the electromagnetic field. In addition to the electromagnetic force on particles and the pressure-gradient force, the effects of particle collisions must be included in this force-balance equation. Since collisions are between two particles, the collisional coupling is proportional to e^2 and n^2. Since electron-electron collisions and ion-ion collisions conserve momentum, only electron-ion collisions contribute to resistivity. Hence the resistive force is also proportional to the relative velocity of electrons and ions:

$$\mathbf{F}_{\text{resistive}} = \eta e^2 n^2 (\mathbf{v_i} - \mathbf{v_e}) \tag{3.9}$$

If we say that the only forces in our charged fluid are $\mathbf{F}_{\text{Lorentz}}$ and $\mathbf{F}_{\text{resistive}}$ then our approximation is called the *resistive MHD approximation*. Defining $\mathbf{V} = \mathbf{v}_i - \mathbf{v}_e$ and $\mathbf{J} = en\mathbf{V}$, we can write this coupling as

$$\mathbf{E} + \mathbf{V} \times \mathbf{B} = \eta \mathbf{J} \tag{3.10}$$

Equation (3.10) is often called the *resistive Ohm's law*. If we go even further and assume that the fluid is perfectly conducting, i.e. $\eta = 0$, we get the *ideal Ohm's law*:

$$\mathbf{E} + \mathbf{V} \times \mathbf{B} = 0 \tag{3.11}$$

What is surprising about this equation is that the flow velocity in the directions perpendicular to the magnetic field is fixed by the electric and magnetic fields. Equation 3.11 is mathematically equivalent to

$$\mathbf{V}_\perp = \frac{\mathbf{E} \times \mathbf{B}}{B^2}. \tag{3.12}$$

Finally, to complete the set of MHD differential equations it is necessary to include Maxwell's equations, which are given in Chapter 3.2.

3.1.1 Alfvèn Waves

Studying waves in plasma is like going to the zoo. There are as many species of waves as animals, including but not limited to plasma oscillations, acoustic waves, light waves, cyclotron waves, and hydromagnetic waves. Some waves aggressively propagate instabilities, some are small and quick, and some need to be coaxed with very specific habitats.

Alfvèn waves the elephant of plasma waves. They are low frequency oscillations, in which the entire plasma oscillates, field and fluid as one. Specifically, they are the hydromagnetic waves that travel along magnetic field lines. They propagate at the characteristic Alfvèn speed:

$$v_{\mathrm{A}} = \frac{B}{\sqrt{\mu_0 \rho}}. \tag{3.13}$$

Alfvèn waves are especially important in the MHD framework and interesting for plasmas which, like SSX, have strong magnetic fields.

3.2 Frozen-in Flux

The ideal MHD equation has a beautiful consequence that is a great aide to the visualization of plasma. This consequence is the frozen-in flux constraint, which says essentially that magnetic flux is frozen into a plasma fluid. The frozen-in flux constraint is easy to derive. We follow [42]. Maxwell's laws in SI units are

$$\nabla \cdot \mathbf{E} = \frac{\rho}{\epsilon_0} \tag{3.14}$$

$$\nabla \cdot \mathbf{B} = 0 \tag{3.15}$$

$$\nabla \times \mathbf{B} = \mu_0 \mathbf{J} \tag{3.16}$$

$$\nabla \times \mathbf{E} = -\frac{\partial \mathbf{B}}{\partial \mathbf{t}} \tag{3.17}$$

We neglect the displacement current correction in Ampere's law, because the time scale of diffusion in plasma is much longer than the time scale of light to propagate in the plasma.

According to the resistive MHD approximation,

$$\mathbf{E} + \mathbf{v} \times \mathbf{B} = \eta \mathbf{J} \tag{3.18}$$

Let us use Maxwell's equations to eliminate all variables from this equation except $\mathbf{B}$. We can substitute Ampere's law into this equation to eliminate $\mathbf{J}$:

$$\mathbf{E} = -\mathbf{v} \times \mathbf{B} + \frac{\eta}{\mu_0} \nabla \times \mathbf{B} \tag{3.19}$$

To eliminate E, we take the curl of this equation and use Faraday's law to get

$$\frac{\partial \mathbf{B}}{\partial t} = \nabla \times \mathbf{v} \times \mathbf{B} + \frac{\eta}{\mu_0} \nabla^2 \mathbf{B} \tag{3.20}$$

Equation 3.20 is called the magnetic induction equation. Before we use it to derive the frozen-in flux condition, we must retreat back to ideal MHD, which means the diffusion term ($\frac{\eta}{\mu_0} \nabla^2 \mathbf{B}$) of the magnetic induction equation goes away and we are left with

$$\frac{\partial \mathbf{B}}{\partial t} = \nabla \times \mathbf{v} \times \mathbf{B}. \tag{3.21}$$

In precise terms, the frozen-in flux constraint says that, in the framework of ideal MHD, the flux across a surface S bounded by a curve l, which moves with the plasma at the fluid velocity V, is constant in time. In other words, we want to show that the time-derivative of this flux is 0.

$$\frac{\mathrm{d}}{\mathrm{d}t} \int_S \mathbf{B} \cdot \mathrm{d}\mathbf{a} = \int_S \frac{\mathrm{d}}{\mathrm{d}t} (\mathbf{B} \cdot \mathrm{d}\mathbf{a}) \text{ (interchange of limits)} \tag{3.22}$$

$$= \int_S \frac{\partial \mathbf{B}}{\partial t} \cdot \mathrm{d}\mathbf{a} + \int_{\frac{\mathrm{d}S}{\mathrm{d}t}} \mathbf{B} \cdot \mathrm{d}\mathbf{a} \text{ (Leibniz Rule)} \tag{3.23}$$

$$= \int_S \nabla \times (\mathbf{v} \times \mathbf{B}) \cdot \mathrm{d}\mathbf{a} + \int_{\frac{\mathrm{d}S}{\mathrm{d}t}} \mathbf{B} \cdot \mathrm{d}\mathbf{a} \text{ (substituting equation 3.21)} \tag{3.24}$$

$$= \int_S \nabla \times (\mathbf{v} \times \mathbf{B}) \cdot \mathrm{d}\mathbf{a} + \int_{\mathrm{d}S} \mathbf{B} \cdot (\mathbf{v} \times \mathrm{d}\mathbf{l}) \tag{3.25}$$

$$= \int_S \nabla \times (\mathbf{v} \times \mathbf{B}) \cdot \mathrm{d}\mathbf{a} + \int_{\mathrm{d}S} (\mathbf{B} \times \mathbf{v}) \cdot \mathrm{d}\mathbf{l} \text{ (vector identity)} \tag{3.26}$$

$$= \int_S \nabla \times (\mathbf{v} \times \mathbf{B}) \cdot \mathrm{d}\mathbf{a} - \int_{\mathrm{d}S} (\mathbf{v} \times \mathbf{B}) \cdot \mathrm{d}\mathbf{l} \text{ (Cross-product is anticommutative)} \tag{3.27}$$

$$= \int_{\mathrm{d}S} (\mathbf{v} \times \mathbf{B}) \cdot \mathrm{d}\mathbf{l} - \int_{\mathrm{d}S} (\mathbf{v} \times \mathbf{B}) \cdot \mathrm{d}\mathbf{l} \text{ (Stoke's theorem)} \tag{3.28}$$

$$= 0 \tag{3.29}$$

Thus the flux across our surface S, which is moving with the plasma, is constant in time. If we consider the limiting case of shrinking the tube smaller and smaller, the tube will eventually become a field line. Since we picked the flux tube to follow the plasma velocity, the shrunk tube is also a flow line for the fluid.

3.3 Sweet-Parker Magnetic Reconnection

The frozen-in flux constraint can be violated. An important violation is magnetic reconnection. In magnetic reconnection, magnetic field lines are broken and reformed, as shown in figure 3.1. Here, a $+\hat{\mathbf{x}}$ directed $\mathbf{B}$ field sheet is flowing in the $+\hat{\mathbf{y}}$ direction from the $-\hat{\mathbf{y}}$ axis, and a $-\hat{\mathbf{x}}$ direction $\mathbf{B}$ field is flowing in from the opposite side. If magnetic flux were frozen into the fluid at the meeting plane, one sheet would insist the flux be $+\hat{\mathbf{x}}$ directed, and the other would insist the flux be $-\hat{\mathbf{x}}$ directed. Magnetic flux cannot be frozen in the reconnection plane!

How can we explain a violation of this sort? Since the frozen-in flux constraint relies on the ideal MHD equation 3.11, we must look for large violations of this equation in order for the frozen-in flux constraint not to be a mathematical necessity.

The Sweet-Parker model for magnetic reconnection postulates that the important violation of the ideal MHD equation is that it neglects the resistivity of the plasma. Hence the Sweet-Parker model draws its conclusions from the framework of resistive MHD (equation 3.10). The other principal assumption of the Sweet-Parker model is that reconnection is an inherently 2-dimensional process. Ultimately, we would like our reconnection model to describe the physics of two merging spheromaks. However, since the Sweet-Parker model is essentially 2-dimensional, we can simplify the geometry, and consider instead the merging of two oppositely magnetized sheets of plasma.

However, it is important to bear in mind that, while the most famous, the Sweet-Parker reconnection model is one of many models. It explains magnetic reconnection, but often reconnection occurs anomalously quickly in experiment. Reconnection models are generally sorted into the categories collisionless or collisional, depending on the mean-free path of the plasma to which they are applicable. The various reconnection models each include a discarded term in the ideal Ohm's law (equation 3.11), such as the Hall term.

Following the treatment of [3], let the two sheets of width $2L$ merge from the $\pm\hat{\mathbf{x}}$ directions. This is shown below in figure 3.1. There are two regions in this process: the reconnection layer of width 2δ, and the non-reconnection layer.

Resistive MHD Condition

Let us apply the resistive MHD approximation 3.10 separately to these two regions.

Outside the region, the field lines are linear, which means that

$$\nabla \times \mathbf{B} = 0 \tag{3.30}$$

.

From Ampr̀e's law, 3.30 implies that $\mathbf{J} = 0$ and the z-component of 3.10 becomes

$$E_z + v_{in} B_x = 0 \text{ (outside the reconnection layer).} \tag{3.31}$$

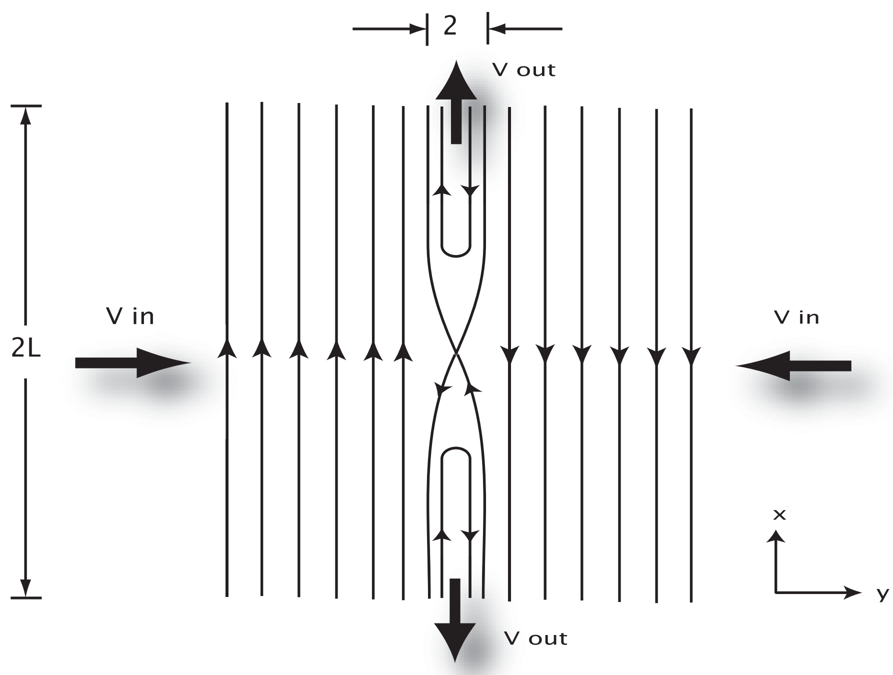

Figure 3.1: The Sweet Parker Reconnection Mode. The small arrows are magnetic field lines, and the large arrows are flow velocities. Opposing **B** fields flow inwards from the $\pm\hat{\mathbf{y}}$ directions. The reconnection outflow is in the $\hat{\mathbf{x}}$ directions.

Inside the reconnection layer, we cannot neglect the current $\mathbf{J}$, because the magnetic field lines are not nearly straight. However, since the two slabs of incoming velocity vectors oppose each other, a good approximation to make in the reconnection layer is stagnation: that $v_{\text{in}} = 0$. Hence, 3.10 becomes

$$E_z = \eta J_z \text{ (inside the reconnection layer).} \tag{3.32}$$

An important question to ask is whether E_z in equations 3.31 and 3.32 is the same E_z. The answer is yes. This is because reconnection is a steady-state process: as long as there is a steady supply of magnetic field lines flowing inward, the picture will look the same. Faraday's law then implies that

$$\nabla \times \mathbf{E} = \frac{\partial \mathbf{B}}{\partial t} = 0. \tag{3.33}$$

$\mathbf{E}$ is curl-free. Consequently, $\mathbf{E}_z$ is the same both inside and outside the reconnection layer.

Conservation of energy $\Rightarrow$ Outflow Speed

If in the Sweet-Parker model there is a steady-state inflow of magnetic fields that are being annihilated, there must be an energetic perpendicular outflow for energy balance. This is shown in figure 3.1. This allows us to calculate the perpendicular outflow velocity:

$$\frac{B_x^2}{2\mu_0} = \frac{\rho v_{out}^2}{2} \tag{3.34}$$

$$v_{out} = \frac{B_x}{\sqrt{\mu_0 \rho}} \tag{3.35}$$

Comparing equation 3.35 with 3.13, we see that

$$v_{out} = v_{\text{A}}. \tag{3.36}$$

The reconnection outflow velocity is the Alfvèn speed.

Continuity Condition

The continuity condition is simply the conservation of mass in an incompressible fluid. In our simple reconnection process, this condition is

$$v_{in} L = v_{out} \delta \tag{3.37}$$

Ampère's law

Now let us apply Ampère's law $\int \mathbf{B} \cdot \mathrm{d}\mathbf{l} = \mu_0 I$ to a rectangular loop about the reconnection layer:

$$B_x(4L) = \mu_0 J_z (2L)(2\delta) \tag{3.38}$$

$$B_x = \mu_0 J_z \delta \tag{3.39}$$

Inflow Speed

The inflow speed can be calculated from our application of the Resistive MHD condition, the continuity condition, and Ampre's law:

$$v_{in} = \frac{E_z}{B_x} \text{ (3.31)} \tag{3.40}$$

$$= \frac{\eta J_z}{\mu_0 J_z \delta} \text{ (3.32 and 3.39)} \tag{3.41}$$

Consequently we have

$$\frac{v_{in}\mu_0\delta}{\eta} = 1. \tag{3.42}$$

The quantity on the LHS of this equation is called the magnetic Reynold's number R_m.

Combining our expressions for inflow and outflow speed, we have the important relationship

$$\frac{v_{in}}{v_{out}} = \frac{1}{\sqrt{S}}, \tag{3.43}$$

where the Lundquist number S is defined as

$$S = \frac{v_{\text{Alfvèn}}\mu_0 L}{\eta}. \tag{3.44}$$

Chapter 4

Design of The Soft X-Ray (SXR) Detector

We have seen now that the reconnection event annihilates the opposing magnetic fields on the spheromaks. The $\frac{B^2}{2\mu_0}$ magnetic energy density does not disappear, but rather gets converted into other forms, namely photons, heat, flow, and energetic ions. Naturally we would like to measure all of these quantities.

What makes a soft x-ray detector such an excellent diagnostic for a reconnection event is that it measures two of these four quantities (energetic photons and heat). Not only does it provides a wealth of information on the flux and spectral distribution of energetic photons but, since the distribution of photons is a function of temperature, a temperature measurement can be gleaned from the soft x-ray detector.

”Soft x-ray” is a synonym for extreme ultraviolet light, i.e. for light in the 10 eV to 150 eV range. A perfect soft x-ray detector would output the intensity of photons striking the detector at all energies. X-ray spectrometers do exist, but they are not practical for an experiment on the scale of SSX, due to high cost. Our solution was to build an x-ray detector consisting of a set of broadly sensitive photodiodes, each filtered with a different thin metallic foils.

Our foils are made out of Al, Ti, Zr, and In. They are 100 nm thick, except for the Ti filter, which is 50 nm thick. All foils block out low-energy (i.e. visible and below) light, and each foil allows a different band of ultraviolet light to pass through. The result is an x-ray detector that has rough spectral resolution. What we sacrifice with this paradigm is the ability to resolve detailed structures in the spectrum, such as atomic transition lines. What we retain is not only the flux across a broad spectrum of SXR energies, but also information about the plasma temperature, of which the emission spectrum is a function. While the line emission data are useful for the calculation of impurity fractions, such fractions can be calculated using data from our high-resolution vacuum ultraviolet (VUV) spectrometer, which operates at a lower energy level. We also do not sacrifice time-resolution, because the photodiodes are extremely fast (700 ps when properly biased).

Multi-channel x-ray diagnostics are common in plasma devices, their widespread use having been spurred by the development of absolute Si photodiodes. The CDX-U spherical torus at Princeton Plasma Physics Laboratory has a foil-filtered x-ray diagnostic, whose foils are made out of Ti and Be [21]. Another x-ray detector similar to ours is the Madison symmetric torus reversed-field-pinch, which consists of four silicon diodes covered with four different foils [19]. The design of our SXR detector is closely based on one that was built at Caltech [17].

A slightly different but common filter technique is the Ross filter technique, in which the K-edges of two filters of the same material but different thickness are exploited for the measurement of a small band [18]. An example of a K-edge is the Aluminum 72 eV K-edge, which can be seen on figure 4.7. The Ross filter is more appropriate for looking at harder x-rays, where elemental K-edges are more prevalent.

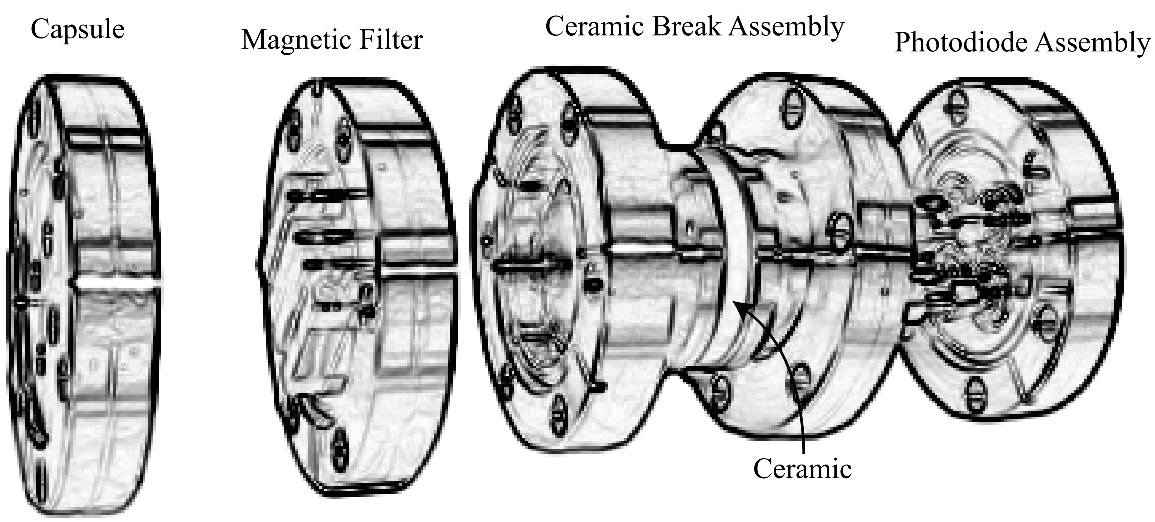

Figure 4.1: Assembly figure of the soft x-ray detector. A particle enters the detector from the left, where it passes through one of four holes on the leftmost conflat, whose purpose is to hold the magnets on the filtering conflat in place. Charged particles are trapped by the filtering conflat, but photons pass through the filter, through the ceramic break, and into one of the four photodiodes screwed onto the rightmost conflat.

4.1 Photodiodes

The SXR detector uses International Radiation Detectors' (IRD) AXUV silicon p-n junction photodiodes. Although AXUV stands for Absolute eXtreme UltraViolet, AXUV diodes are also sensitive to soft x-rays. Their spectral response is the *unfiltered* curve on figure 4.7.

They rely on the internal photoelectric effect [22], which means they are less sensitive to neutral particles than conventional XUV diodes. Additionally, compared to XUV photodiodes, AXUV photodiodes have low noise, do not require a bias voltage, are not affected by magnetic fields, and have a large collection area to size ratio. The specific model of AXUV diodes used in the SXR detector is AXUV-HS5, which has a collection area of 1 mm^2, and a rise time of 700 ps when fully biased at 50 V [22].

When photons of energy 1.12 eV or greater are incident on the an AXUV diode, electron-hole pairs are created. If the photon has greater energy, the number of carriers (electrons and holes) created is very nearly proportional to the photon energy. Put another way, if we define the diode *quantum efficiency* to be the number of carriers created per photon, then we can say that the quantum efficiency is linear. Separated by the p-n junction electric field, the carriers flow through the external circuit. Hence the photodiode can be modeled electrically as a current source.

Spectral calibration of IRD's line of diodes has been performed at the National Synchrotron Light Source at Brookhaven National Laboratory in the 1 eV to 10 keV interval[27]. The responsivity is plotted in figure 4.7.

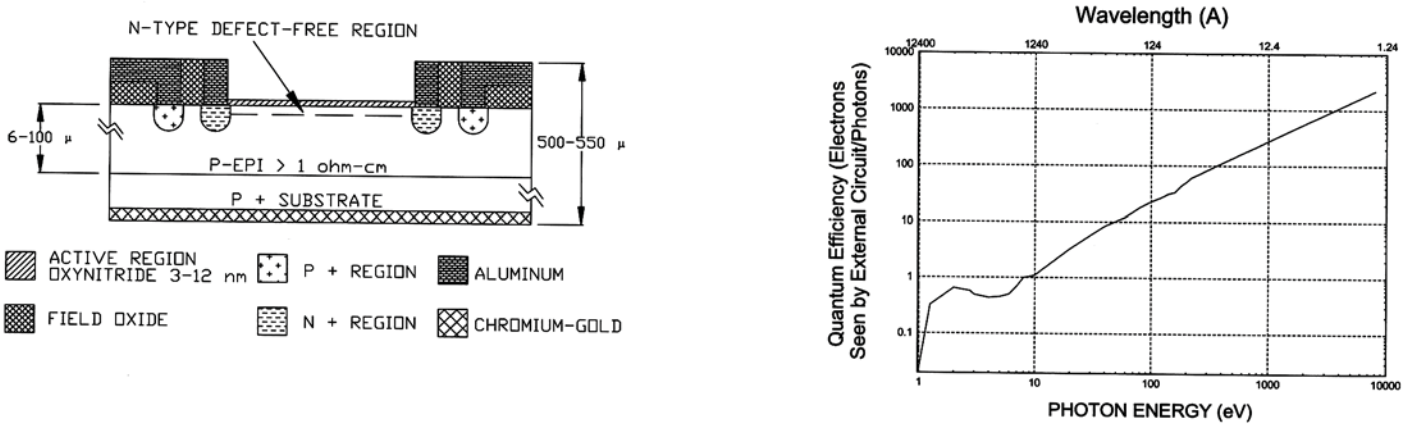

Figure 4.2: *Left:* A schematic of the AXUV series photodiode, taken from the International Radiation Detectors brochure. *Right:* Quantum efficiency of the AXUV photodiodes, again taken from the IRD literature. Above 10 eV, the quantum efficiency is highly linear, approximately $\frac{E_{photon}}{3.63}$.

4.2 Connecting the Photodiodes

Each photodiode has a screw-on foil filter, which are discussed below in 4.4. The photodiodes themselves screw onto a Ceramaseal vacuum feed-thru, mounted on a 2.75" conflat. This conflat is isolated from machine ground with a ceramic break (see figure 4.1). The photodiode assembly is shown in figure 4.4.

The photodiodes, being current sources, are terminated with 50 Ω resistors inside the LeCroy

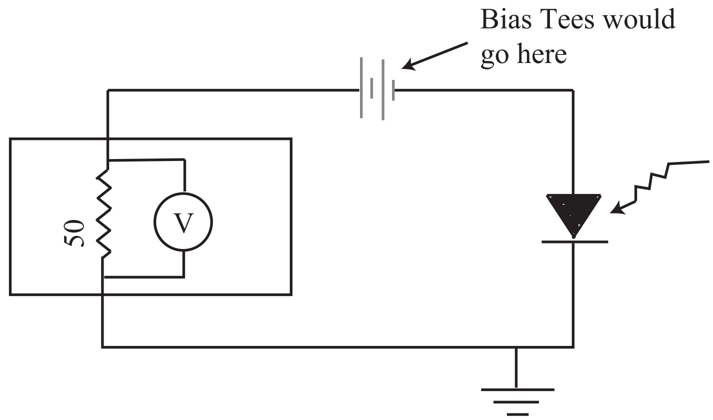

centerline

Figure 4.3: The SXR Detector Circuit. The actual detector has four such circuits, one four each photodiode. The photodiode can be modeled electrically as a current source. The current goes into the magnetically isolated screen room, where it is measured by an oscilloscope, which is in 50 Ω coupling mode.

oscilliscope. To increase the responsiveness of the carriers and hence improve the rise-time, it is often a good idea to bias photodiodes. Bias tees provide a high-quality bias from a low-quality battery voltage. Our original plan was to bias the photodiodes with bias tees (Picosecond Pulse Labs model 5535). However, when the bias tees were in place, cable capacitance distorted the signal. When the bias tees were bypassed, the photodiodes were still responding fast enough for our purposes. Furthermore, the line of photodiodes that we used can be used without bias [22]. Hence we ended up not using the bias tees. The circuit diagram is shown in figure 4.3.

As shown in chapter 7.2, the peak of the photodiode signal ranges from about 30 mV for the aluminum signal down to 1 mV for the zirconium signal. To protect the integrity of these small signals, care is taken in the connections. For maximal insulation from noise, semi-rigid coaxial cable carries the signal to a screen room. Providing the best shielding (better than 110 dB) among all types of coaxial cable , semi-rigid cables have a seamless copper tube as an outer conductor, much like a water pipe. Our semi-rigid cables were 0.141” in diameter and purchased from [28]. Up to the screening room, all connectors are gold-plated SMA, a type of coaxial cable connectors that is compact and high-quality.

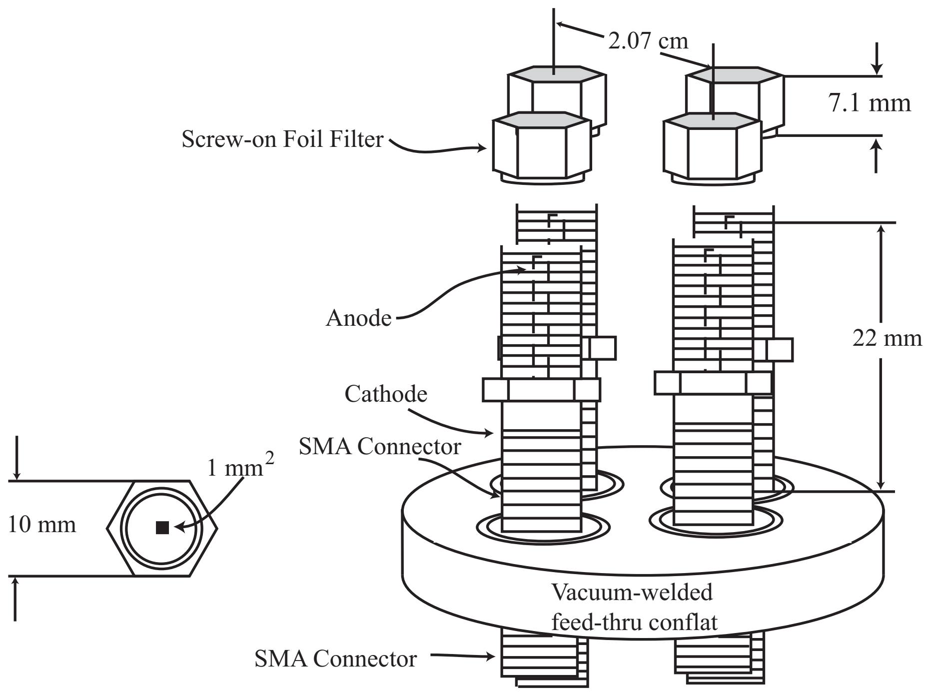

Figure 4.4: The photodiode assembly. *Left:* A bird's-eye view of a photodiode. *Right:* The foil filters screw onto the top of the photodiodes, which screw onto the feed-thru conflat.

4.3 Charged Particle Filter

The problem with putting AXUV photodiodes in the plasma is that they are not plasma-proof. While insensitive to neutral particles, they are sensitive to charged particles, which are sure to be found in a plasma. Hence a charged particle filter is necessary to block the particles from reaching the photodiodes.

The charged particle filter provides a magnetic field that deflects ions and electrons from the photodiodes. Thru-holes allow photons to pass through. Machined at Swarthmore College, the magnetic filter consists of compact but strong Neodymium-Iron-Boron magnets, which provide a measured magnetic field of 0.51 +/- 0.06 T in the thru-holes. To see how the field varies within the thru-hole, a Biot-Savart code extrapolates the measured field at the maximum (the center of the thru-hole) to the rest of the thru-hole. It does this by assuming the magnets have uniform magnetization, and applying the Biot-Savart law to bound surface currents. It is clear from figure (4.5) that this variation is quite small.

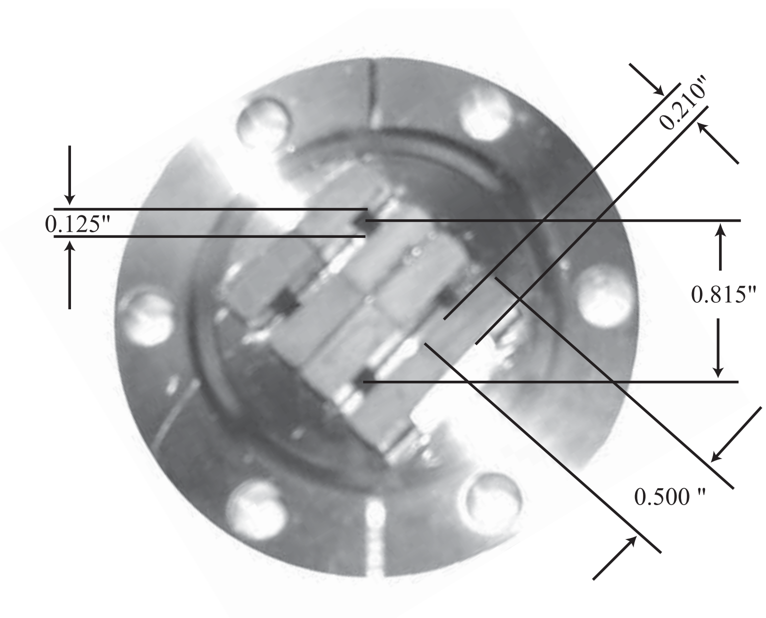

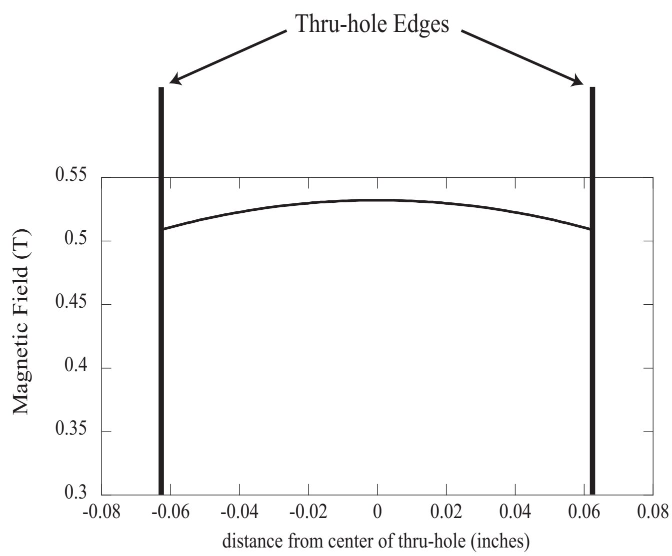

Figure 4.5: *Left:* The charged particle filter. There are four holes that allow photons to pass undeflected through the filter to the photodiodes. Charged particles are trapped by the two magnets surrounding each hole. *Right:* A plot of the variation of the filter magnetic field across the thru-holes on the magnetic axis.

Of course, if a charged particle is fast enough, it can make it through the magnetic field without being sufficiently deflected. If too many particles make it through the magnetic filter, they will distort the SXR signal. Let us see how fast such a particle would need to be.

Since we only need this calculation to order-of-magnitude accuracy, let us simplify the situation by assuming that all charged particles meet the magnetic filter head-on. Then the criterion for a particle to be slow enough to be deflected by the magnetic field is that the diameter of its gyro-orbit fit in the length of the magnetic field:

$$r_{\text{gyro}} < \frac{L}{2} \tag{4.1}$$

The gyroradius of a charged particle in a uniform magnetic field is obtained by attributing the centripetal force of a circling particle to the magnetic field:

$$F_{\text{cent}} = F_B \tag{4.2}$$

$$\frac{mv^2}{r_{\text{gyro}}} = qvB \tag{4.3}$$

$$r_{\text{gyro}} = \frac{mv}{qB} \tag{4.4}$$

Comparing this expression for the gyroradius with the deflection criterion 4.1, and using $L = 0.5$" and $B = 0.5T$, the deflection criterion becomes

$$v_{\text{ion}} < 2.9 \times 10^5 \frac{\text{m}}{\text{s}}, \tag{4.5}$$

$$\text{or } E_{\text{ion}} < 440eV \tag{4.6}$$

for ions. At SSX plasma temperatures of 20-30 eV, the tail of the thermal ion distribution that makes it through the filter will be negligible. However, since SSX is known to have ion beams from reconnection, those could possibly make it through the filter. We need not consider the electrons, since they carry less inertia than the ions and hence are more easily deflectable.

4.4 Foil Filters

The AXUV series photodiodes are sensitive to visible light as well as soft x-rays. Hence this part of their spectrum must be filtered out. Figure 4.6 shows a bird's eye view of the photodiodes covered by their foil filters.

In accordance with the requirement that the SXR detector has a rough soft x-ray spectrum resolution, the four chosen foil filters each pass different very different regions of the SXR region. The four foil filters are Aluminum (100 nm), Zirconium (100 nm), Titanium (50 nm), and Indium (100 nm). Indium is an interesting choice, as its narrow soft band pass around 20 eV is a good complement to the other filters with higher band passes. The response of each filtered diode is plotted in figure 4.7.

The transmission of the foils were calculated using the Lawrence Berkeley National Laboratory website [24]. This calculation proceeds by looking up the two atomic scattering factors f_1 and f_2 for the atom of which the foil is made. These atomic scattering factors

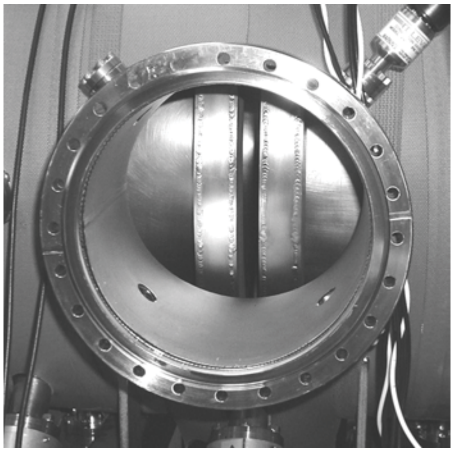 

Figure 4.6: *Left:* A view of SSX as the SXR detector sees it. The detector is normally mounted on the large conflat that is missing in this photo. Inside the vacuum chamber is the flux conserver, which consists of two copper cylinders with a space between them. *Right:* the foil-filtered photodiodes with their screw-on foil filters. Each photodiode has a different foil filter.

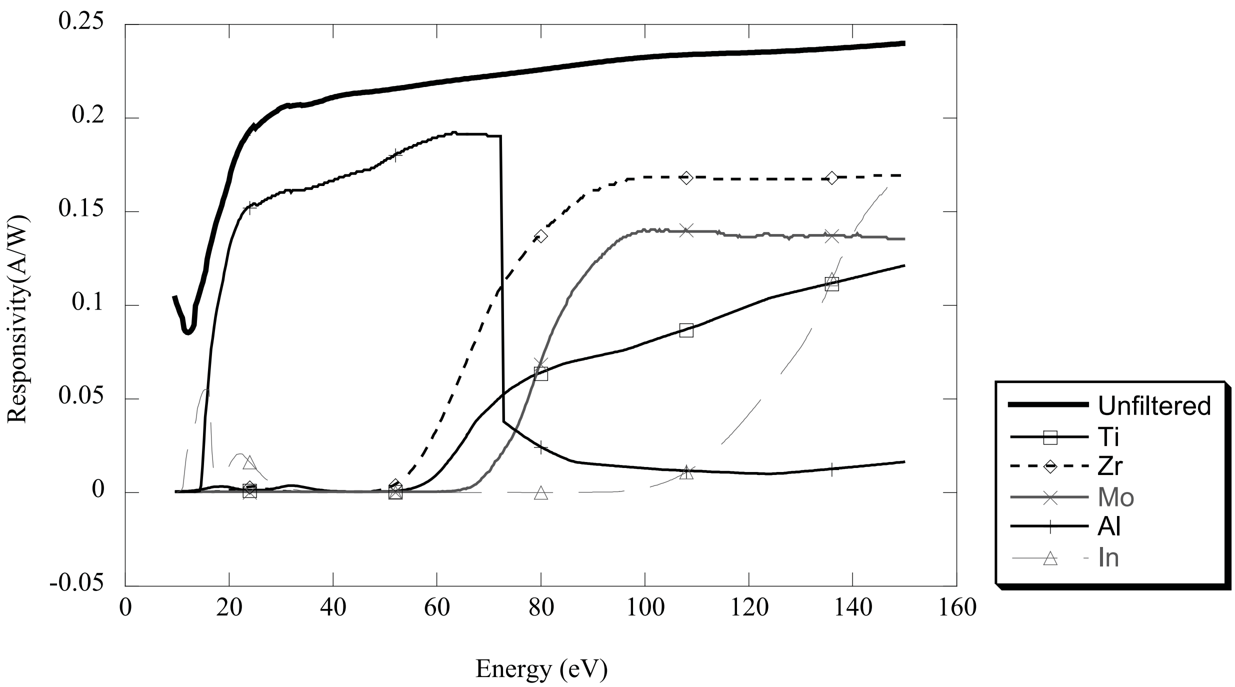

Figure 4.7: Responsivity of photodiodes when filtered. The unfiltered line is just the spectral response of the diodes.

are functions of energy. The atomic photoabsorption cross section μ_a is calculated from f_2 using the relation [24]

$$\mu_a = 2r_0\lambda f_2 \tag{4.7}$$

where r_0 is the classical electron radius, and λ is the wavelength of light. The transmission of x-rays through a foil of thickness d with n atoms per unit volume is then given by

$$T = \exp(-n\mu_a d). \tag{4.8}$$

The atomic scattering factors that the LBNL website uses were verified at [25].

4.5 Pre-installation tests of the Diagnostic

4.5.1 Visible Light Flash Test

Since the SXR detector is designed to look in the soft x-ray range, it ought to be insensitive to visible light. However, the photodiodes themselves do respond to visible light. Hence the foil filters must be capable of filtering out this light.

To test their capability, we measured the response of the four filtered diodes, along with the response of an unfiltered diode, to a camera flash. The camera flash has a duration of approximately 30 μs, a similar time-scale to an actual SSX shot. Additionally, we used the actual SXR detector's semi-rigid cabling and oscilloscopes during this test, to make it as similar as possible to an actual SSX shot (except without the plasma and x-rays!).

The results for the diodes filtered by aluminum, indium, and zirconium were excellent, each of them generating a current that is 3 orders of magnitude less than the current on the unfiltered diode. The test for the titanium-filtered diode is a little concerning, since its current was only 2 orders of magnitude less than the current on the unfiltered diode. It is possible that this discrepancy indicates a pinhole in the foil filter, even though the filter looks intact to the eye. However, it is also possible that, since the titanium filter is thinner than the others (50 nm instead of 100 nm), it simply passes more visible light. Also, since the titanium signal appears to be about the right order of magnitude, it is possible that this pinhole (if it exists) appeared during the last vent.

We can be reasonably confident that the Al, Zr, and In filters are essentially blocking the photodiodes from visible light. As figure 4.8 shows, these filters reduce the visible light by a factor of 1000. Figure 5.2 shows that the visible light emission spectrum can be up to 1000 times the intensity of the SXR spectrum, but only in sharp peaks, and usually the discrepancy is not nearly so large.

The SXR detector requires a fast rise time in order to pick out detailed features in the time-evolution of the plasma. However, the SXR data is averaged in 100-point blocks over a period of 1 μs to rid the signal of noise. Thus a rise time significantly faster than that will not improve the quality of the data much. According to its specifications, the photodiodes have a 10-90% rise time of 700 ps when biased with 50 V. We tested the rise time using a simple LED apparatus shown in figure (4.9).

The results of the test are shown in figure (4.9). For reasons explained in section (4.2), we ended up not biasing the photodiodes when we used them in SSX. However, as the results of this test show, the bias tees do not improve the magnitude of the photodiode signal and, while they do improve the rise time, 200 ns is fast enough if we are looking at the data in 1 μs bins. Since the speed of the pulse generator was not investigated, the 200 ns rise time should be taken as an upper limit.

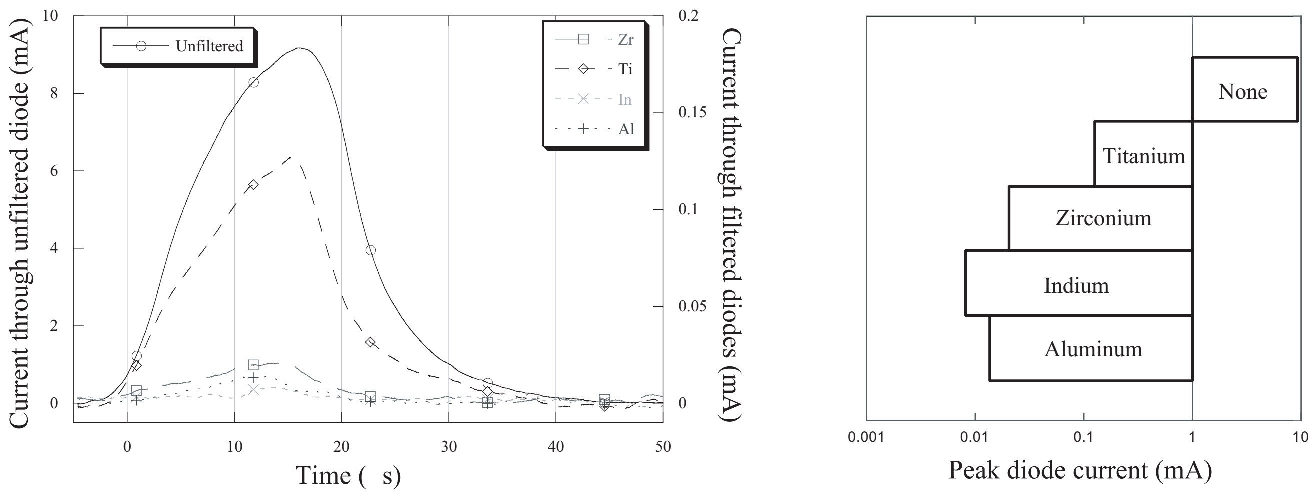

Figure 4.8: Left: Current generated by the variously filtered photodiodes in the flash test. Right: A comparison of the peak currents in this experiment.

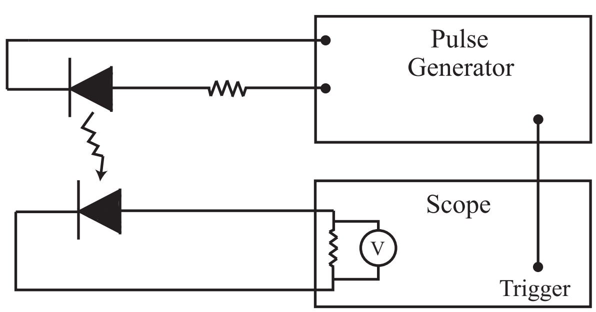

	Signal Strength	Rise Time
0 V Bias	120 V	200 ns
9 V Bias	100 V	50 ns

Figure 4.9: *Left:* Apparatus for testing the rise time of the photodiodes. A signal generator pulses an LED. The photodiodes catch this light and push a current through the resistor. The oscilloscope, triggering off the pulse generator, reads the voltage across the resistor. The oscilloscope is terminated at the 50 Ω. *Right:* The rise time and signal strength of the diodes in this test.

Chapter 5

From Soft X-Rays To...

Soft x-rays are generated by two different mechanisms. First, there is the bremsstrahlung continuum, which is the radiation from accelerating charges. Another word for this radiation is free-free emission, since it is emitted by electrons and ions that are not bound to a nucleus. Second, there is line emission, radiated by bound electrons undergoing atomic transitions. Finally, there is the recombination continuum.

5.1 Bremsstrahlung

Accelerating charges radiate. In a hot plasma, this acceleration is due to collisions between electrons and ions, which explains how bremsstrahlung, which is German for "braking radiation," found its name. The basic expression for the radiated power due to a single accelerating charge is [7]

$$P = \frac{\mu_0 q^2 a^2 \gamma^6}{6\pi c}, \tag{5.1}$$

where a is the acceleration of the charge, *etc.* The classical model for bremsstrahlung is an oscillating dipole. Since bremsstrahlung is proportional to the rate of change of the dipole moment, and in collisions between like particles the dipole moment is proportional to the center of mass of the two particles and thus a constant in time, only electron-ion collisions contribute to bremsstrahlung radiation. Due to mismatch in the masses of electrons and ions, electrons move so fast that their motion dominates the bremsstrahlung spectrum and, furthermore, the approximation that the electron sees the ion as a fixed frame of reference throughout the collision is valid. Quantum mechanical corrections for the bremsstrahlung emission are of the same order of magnitude as the classical expression, but they affect the classical result only by a scalar multiple. They are usually conveniently collected into a multiplicative correction called the Gaunt factor and denoted g_{ff}.

The total bremsstrahlung emission is obtained by integrating over 1) the Maxwellian electron velocity distribution, 2) all the possible impact parameters, and 3) the particle distribution in a plasma. In dimensions Power/(cm^3 · Energy), the emission intensity is given by

$$\epsilon = \frac{2^5 \pi e^6}{3mc^3} \sqrt{\frac{2\pi}{ekmT}} Z^2 n_e n_i e^{-\frac{h\nu}{kT}} g_{ff}. \tag{5.2}$$

5.2 The Rest of the Emission Spectrum

If the SSX plasma was purely 100% ionized hydrogen, the continuum would be the end of the story. Since this is not true of SSX or any other plasma, it is necessary to consider the radiation from atomic transitions. As figure (5.2a) shows, even if the plasma is pure hydrogen, a significant portion of the emission spectrum is due to recombination. In general, line radiation from very small amounts of impurities, even less than 1% by molarity, overwhelm the bremsstrahlung emission spectrum (see figure (5.2b). Furthermore, impurities can affect the bremsstrahlung curve itself, due to the Z-dependence of equation 5.2, though this effect is small for plasmas like SSX with low impurity fractions.

The impurity content of SSX is very small, but nevertheless significant. A residual gas analyzer measures the partial pressure of residual gases in the SSX plasma, but this diagnostic can only be used between SSX shots. From the residual gas traces (see figure 5.1), we conclude that, when idle, the residual gas in SSX is largely H_2, with significant amounts also of water, carbon, and some nitrogen. Since the hydrogen that is puffed into the vacuum chamber and ionized is 99.9995% pure, and the pressure of hydrogen pumped into the chamber is about 10,000 times the vacuum pressure (2×10^{-7} torr), the residual gas in SSX is negligible. However, the actual impurity content when running is likely to be higher, as energetic charged particles striking the chamber walls are likely to release impurities loosely imbedded in the walls. VUV spectrometry indicates that the impurity content of carbon and oxygen is likely to be a few percent of each [43]. As figure 5.1 shows, any carbon during an SSX shot is liberated from the vessel walls by the plasma.

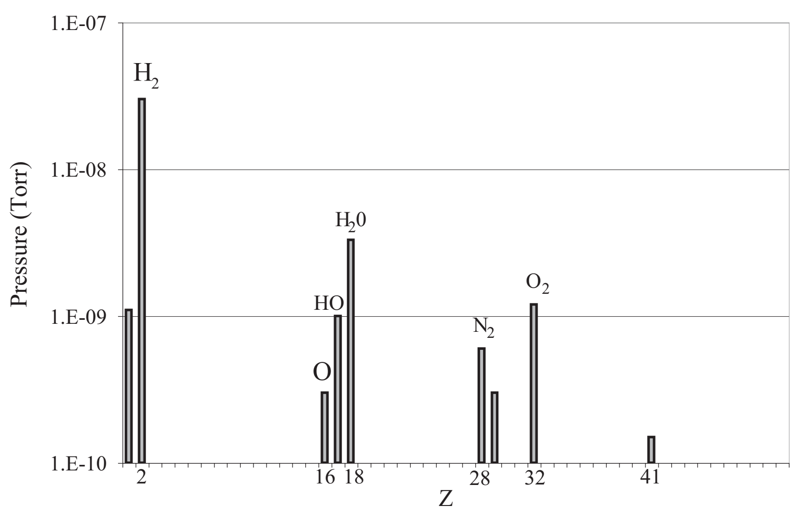

Figure 5.1: The residual gas in SSX.

5.2.1 Spect3D

Spect3D is a third party plasma modeling software package published by Prism Computational Sciences, Inc [26]. It allows us to calculate the emission spectrum of a plasma, so that there is a reference to which we can compare the (rough) spectrum that the SXR detector measures. The inputs to a Spect3D simulation are plasma size, temperature, density, and atomic makeup. From these parameters, Spect3D calculates atomic level populations and the emergent spectra, along with the bremsstrahlung contribution, assuming collisional/radiative equilibrium. The temperature and density parameters are allowed to be functions of space, but we kept them constant, as space resolved density and temperature measurements are too difficult for us to measure.

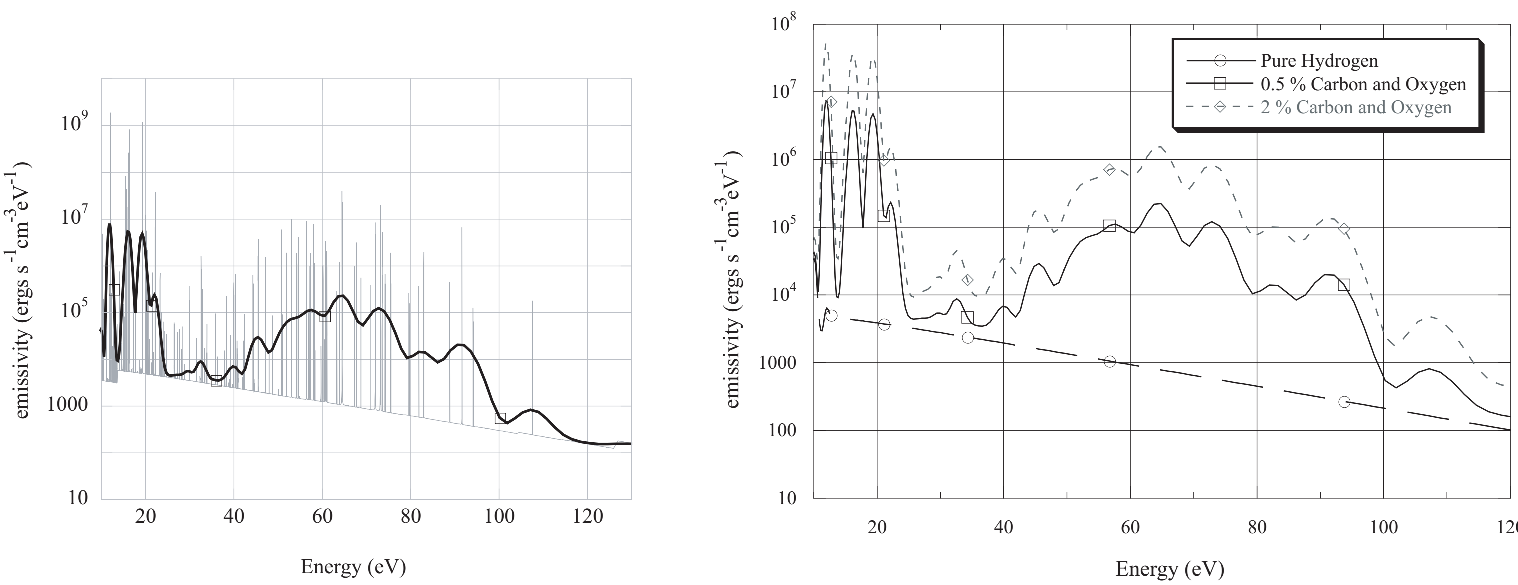

Figure 5.2: The output of the Spect3D model. On the left is a 25 eV, 10^{15} cm^{-3} hydrogen plasma with 0.5% each of carbon and oxygen. Both the line radiation and the Bremmstrahlung continuum can be seen. The black curve is the spectrum when the line radiation is smoothed. On the right is the output of the same Spect3D model, except the impurity fractions are varied.

Before being fed to the temperature-fitting analysis, the line emission, which comes in very strong and very narrow discrete energy widths, is smoothed (in a way that keeps $\int \epsilon \mathrm{d}E$ constant in a neighborhood about each energy value).

5.3 Temperature-Fitting Analysis

5.3.1 Forward Modeling

The simplest approach to analyzing the soft x-ray data would be to try to reconstruct the soft x-ray spectrum from the four soft x-ray measurements at each time point. Then, this spectrum could be compared to ideal spectra generated by Spect3D or the Brehmsstrahlung emission equation (5.2). If the reconstructed spectrum has enough detail, the fruit of this comparison would be dynamic values for plasma temperature and impurity content.

Unfortunately, this "reconstructed spectrum" is not uniquely determined by this sort of comparison. In fact, armed with only four soft x-ray measurements at each time point and the responsivity curves of the diodes (see figure 4.7), attempting to directly reconstruct the spectrum is a losing battle.

A more bountiful approach is a technique called forward modeling. Instead of asking "what do our soft x-ray measurements say the spectrum should be?" we ask "assuming we know the plasma temperature and impurity content, what should the soft x-ray detectors see?" The latter question is definitely answerable, given the responsivity curves of the diodes (4.7) and a spectrum calculated either from the Brehmsstrahlung equation (5.2) or by Spect3D (if we want to include the effects of impurities). We then compare the simulated diode "measurements" to the real diode measurements, and adjust the temperature and impurity content to optimize the fit.

In practice, we do not try to adjust the impurity content dynamically (at each time point), but rather we just make an impurity *ansatz* at the beginning of the calculation. Additionally, we allow the fitting procedure to determine a normalization constant that essentially sets the density and volume of plasma that the simulated diodes see. This normalization constant is actually directly calculable from the density of the plasma and geometric considerations (see appendix), but in practice the fitting procedure does a better job. Since the normalization constant is not a dynamic variable, we run the fitting procedure in two stages. The first stage adjusts both the temperature and normalization constant for the best fit between the simulated and real SXR measurements. The second stage takes the normalization constant calculated in the first stage as a known quantity and adjusts only the temperature to fit. Adjusting the normalization constant is essentially equivalent to adjusting the plasma density, since for both bremsstrahlung and line radiation, there is a nearly exact proportionality:

$$\epsilon \propto n^2. \tag{5.3}$$

The only problem with this procedure is that if there is a time-dependent density (which there is!), then from looking at the SXR signals alone, we cannot say whether a changing signal is from a changing temperature or a changing density. The solution is to use the density trace from the He-Ne interferometer and equation 5.3. If we divide the SXR signals by the time-dependent density trace-squared, then the SXR signals that the temperature analysis uses are effectively what the SXR signals would be if the density were constant.

Since global scale factors do not affect the temperature-fitting analysis, this procedure is acceptable.

We can formulate our fitting problem as trying to pick a vector $\mathbf{x}$ that achieves the vector relation $\mathbf{y} = f(\mathbf{x})$. That is, to pick $\mathbf{x}$ such that $\| f(\mathbf{x}) - \mathbf{y} \|$ is minimized. In our case, $\mathbf{x}$ is the 2D vector (temperature,density). The function $f : \Re_+ \to \Re_+^4$ is a composition of two functions $f = p \circ s$. The function $s : \Re_+^2 \to \mathcal{F}(\Re_+)$ is the output of the Spect3D simulations, which gives the emission spectrum as a function of plasma temperature and density. The function $p : s(\Re_+^2) \to \Re_+^4$ computes the expected signal in each photodiode from the simulated spectrum that Spect3D outputs and the responsivity of the photodiodes. Mathematically,

$$p_i = \int_0^\infty \epsilon(E)\mathrm{r}_i(E)\mathrm{d}E, \tag{5.4}$$

where r_i is the responsivity of the i^{th} diode. Finally, $\mathbf{y}$ is a set of the four actual signals measured by the photodiodes.

5.3.2 Levenberg-Marquardt Method

The Levenberg-Marquardt Method is one of the most frequently used and arguably the fastest non-linear least-squares fitting method in a wide variety of contexts. Its celerity is due to the fact that it is really a compromise between two different algorithms. The first is Newton's Method, to assume that the function f is a linear, in which case the minimum can be found in one step. Newton's method is excellent near a minimum, where f is nearly linear. The second method is the steepest-descent method, which amounts to "sliding" down the gradient of the error function in parameter space. This method is not especially fast, but it is guaranteed to move closer to a minimum, provided the step size is small enough.

If the current guess for the minimum is $\mathbf{x}$, the Levenberg-Marquardt update formula is

$$\Delta\mathbf{x} = -\left(J^t J + \lambda I\right)^{-1} J^t \mathbf{e}, \tag{5.5}$$

where $\mathbf{e}$ is the vector of errors, J is the derivative matrix of these errors, and λ is a control parameter. The first term on the right-hand side of equation (5.5) represents the Newton's method contribution to the update, and the second is the steepest-descent term. That is, if $\lambda = 0$, then the update is purely Newton's method. As $\lambda \to \infty$, the step size gets smaller and more in the gradient-descent direction. Hence the control parameter λ determines both the relative contribution of each algorithm and the step-size of the update. The Levenberg-Marquardt algorithm adjusts λ at each step. Updates are only accepted if they improve the error, in which case λ is decreased by a factor of 10, under the presumption that the error improvement means that $\mathbf{x}$ is approaching the linear region around the minimum, where Newton's method is more appropriate. If an update is rejected, λ is increased by a factor of 10.

Our fitting algorithm gives more weight to more reliable data points. In precise terms, "weight" means the square of the inverse of the uncertainty of a data point. We took the standard deviation of the noise in a neighborhood of a point to be its uncertainty, and each data "point" is really the time average of the oscilloscope trace in a small neighborhood, and each neighborhood is 1 μs. Also, part of the fitting algorithm feedback is an uncertainty for each calculated temperature.

Chapter 6

The Mach Probe

The Mach probe diagnostic is a variation on the Langmuir Probe. The Langmuir Probe is the simplest possible plasma diagnostic, a simple metal rod which, when exposed to the plasma, can be biased to collect either electrons or ions. A calculation based on the collected current versus bias voltage yields both the plasma density and the plasma temperature.

The concept underlying the Mach probe is elementary. Suppose we wanted to measure the migration of small fish in the ocean, without measuring the velocity of each individual fish. An ingenious method would be to bind two sharks together tail-to-tail, place them in the ocean, and let fish swim into their mouths. Assuming that they have the same size mouth and that they are equally hungry, we could measure the amount of waste each shark produces and know that the shark producing more waste is facing against the fish current.

Suppose you want to measure not the migration of fish, but the ion drift velocity in plasma. Following the shark gluing paradigm, you could assemble a set of two Langmuir Probes, each of which is partially blinded so that it can collect particles from only a specific direction. Apply a negative bias to both probes so that they collect ions. If there is no ion drift velocity, then they will both collect the same current (assuming that they "see" the same solid angle). However, if the plasma has a drift velocity with a nonzero component along the vector connecting the two Langmuir probes, then the upstream probe will collect more current than the downstream probe. Thus the ratio of currents collected by the Mach probe yields information about the ion drift velocity.

The simplicity of the qualitative connection between the ratio of currents and the ion drift velocity belies the theoretical difficulty posed by the quantification of this relationship. Models used to quantify the relationship can be divided into roughly two categories: those that apply to "un-magnetized" plasma, in which the ion gyroradius is larger than the characteristic dimension of the probe, and those that apply to "magnetized" plasma, which assume the opposite limit. The theory for the magnetized model is more or less complete [35], largely due to the fact that large-scale plasma devices like tokamaks operate in this regime. The Mach probe theory for unmagnetized plasma is not as completely developed.

One common feature of all the models, however, is that they are all calibrated to yield not the ion drift speed itself, but the ion drift Mach number. The Mach number M corresponding to a velocity v is the ratio of that velocity to the sound speed:

$$M = \frac{v}{c_{\mathrm{s}}}. \tag{6.1}$$

The sound speed in plasma is $c_{\mathrm{s}} = \gamma\sqrt{\frac{T_e+T_i}{m_i}}$. This is not to be confused with the ion thermal speed $v_t = \sqrt{\frac{T_i}{m_i}}$. In this section we will consistently absorb Boltzmann's constant k into the temperature, which is a common maneuver in plasma physics.

6.1 Drifting Maxwellian Model

Another approach to the Mach probe calibration question would be simply to assume that the only effect of the negative potential to which the component Langmuir probes are charged is to preclude electrons from being picked up by these probes. That is, to assume that the ions have a constant density and are distributed in a drifting Maxwellian everywhere, including near the probe. In this model, the ratio of currents is [31]

$$R = \frac{e^{-W^2} + W\sqrt{\pi}[\mathrm{erf}(W) + 1]}{e^{-W^2} + W\sqrt{\pi}[\mathrm{erf}(W) - 1]} \tag{6.2}$$

where $W = M_{\mathrm{drift}}\sqrt{\frac{T_e+T_i}{2T_i}}$. For small M_{drift}, this expression can be approximated as

$$K = \sqrt{2\pi\frac{T_e + T_i}{T_i}}M_{\mathrm{drift}} \tag{6.3}$$

.

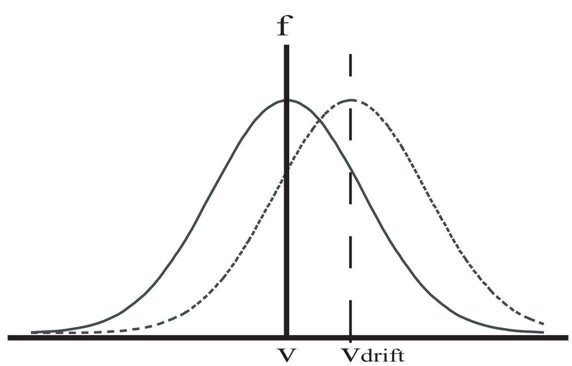

Figure 6.1: Two Maxwellian velocity distributions. The solid distribution is centered around 0 and hence has no velocity drift, whereas the hatched distribution is centered around a finite drift velocity.

6.2 Hudis-Lidsky Model

The Hudis-Lidsky model has been the most frequently invoked model for a Mach probe in unmagnetized plasma. A fluid approach, this model rests on several assumptions [30].

1. That the Debye length is very small compared to the probe radius: $\lambda_D \ll r_p$. This is a pretty safe assumption, as the Debye length in a plasma is normally extremely small. In SSX, it is about 1 μm.

2. That the probe radius is smaller than the ion Larmor radius: $r_p < r_{L,i}$. This is the "unmagnetized" assumption.

3. That the plasma is collisionless (probe radius $\ll$ mean free path and high-density ($\lambda_d \ll$ characteristic probe dimension).

4. That the important physics of the Mach probe can be captured in a one-dimensional model.

5. That the ion temperature is small compared to the electron temperature: $T_i \ll T_e$. Note that this assumption already invalidates the Hudis-Lidsky model for use in SSX, where $T_i \approx T_e$.

6. The Bohm Sheath criterion. Recall that the sheath is the region within one Debye length of a charge inserted into a plasma, that is, the non-neutral region about a perturbing charge. The Bohm Sheath criterion follows from the continuity equation in plasma (equation 3.7), and it states that ions must enter the sheath with kinetic energy greater or equal than the sound velocity:

$$v_i > c_s(\text{at sheath edge}) \tag{6.4}$$

In order for ions to be accelerated to this velocity, there must be a nonzero electric field *outside* the sheath of the probe. This region is called the pre-sheath region, and it typically extends 20 to 50 Debye lengths into the plasma [30].

The Hudis-Lidsky model essentially assumes that ions are flowing at the ion thermal speed v_t far from the probe. As they approach the probe, they acquire an incoming kinetic energy equal to its change in potential energy, to satisfy 1D energy conservation. The pre-sheath region around the probe must be large enough so that ions have reached the sound speed by the time they enter the sheath (Bohm sheath criterion). All ions entering the sheath region are collected into the probe.

the Hudis-Lidsky Mach probe model predicts that the ratio of current collected upstream to current collected downstream is [30]

$$R = \frac{i_{\text{up}}}{i_{\text{down}}} = \exp\left(4\sqrt{\frac{T_i}{T_i + T_e}} M_{\text{drift}}\right) \tag{6.5}$$

.

Note that the commonly used "quotation" of this equation in [31] is incorrect by a factor of 2 (if $T_i \ll T_e$) or $\sqrt{2}$ (if $T_i \approx T_e$) .

If we were to forget about the $T_i \ll T_e$ hypothesis and apply the Hudis-Lidsky model to SSX, where $T_i \approx T_e$, we would have (from equation 6.5):

$$R = 2\sqrt{2}M_{\text{drift}}. \tag{6.6}$$

6.3 Problems with the Hudis-Lidsky Model

The Hudis-Lidsky analysis is an alluring model, incorporating as it does several important principles from plasma physics into a single easy-to-use equation (equation 6.5). Furthermore, it does indeed predict drift velocities that match-up reasonably well against data from other diagnostics [32] [33].

Unfortunately, its ostensible veracity is only a coincidence. As I. Hutchinson explains in [29], it is only a heuristic. Being entirely one-dimensional, the Hudis-Lidsky model assumes that an ion acquires an incoming kinetic energy equal to its change in potential energy, as is true in one-dimension. In two and three dimensions, however, the kinetic energy that the ion picks up can be both in the incoming direction and the transverse direction. Hence, a one-dimensional energy conservation argument cannot produce the correct incoming kinetic energy at the sheath edge.

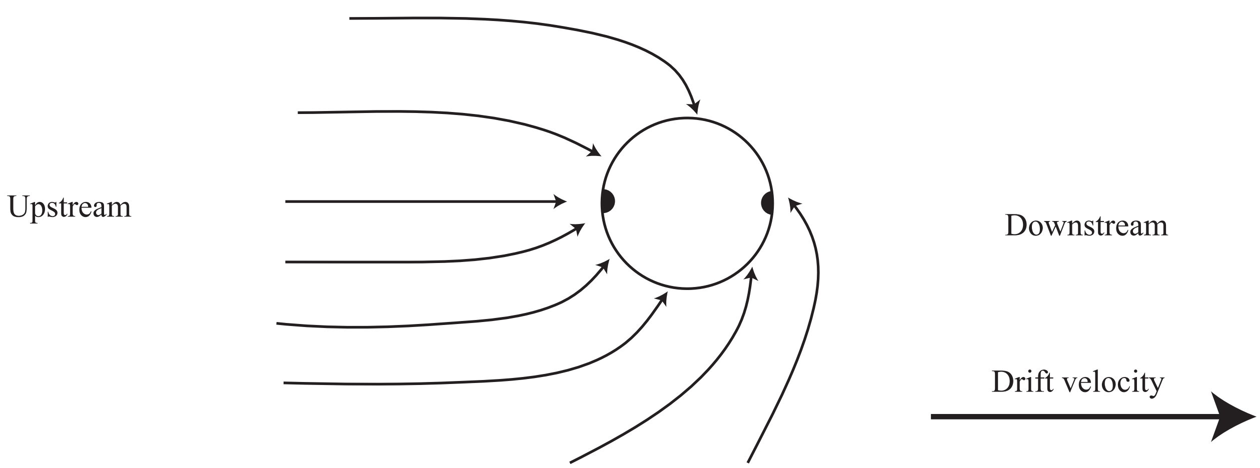

Figure 6.2: Ion collection is inherently multidimensional. As explained in [29], ions can acquire both transverse and incoming kinetic energy as they approach the probe.

After Hudis and Lidsky falsely assume this one-dimensional energy conservation relation, their problems multiply. If there is a velocity drift, then there is a greater incoming kinetic energy on the upstream side, and hence a smaller potential energy drop on the upstream side to conserve energy. Similarly, there must be a larger potential energy drop on the downstream side due to the outgoing drift kinetic energy. However, it is unphysical to suppose that this potential drop is just increased by the amount of the outgoing drift kinetic energy. This is because far from the probe, the plasma must be at the same potential (i.e., if the probe is at the origin, then $\phi_{+\infty} = \phi_{-\infty}$). In a 1D model, there can be a discrepancy in potentials far from the probe, because the negative axis never connects with the positive axis, except through the origin, where the probe is located). In 2 and 3 dimensions this is no longer true. Unless $\phi_{+\infty} = \phi_{-\infty}$, the probe will set up a potential difference arbitrarily far from it. This is cannot be. The Hudis-Lidsky model should be viewed as only a heuristic.

6.4 Particle Simulation

In response to Hutchinson's criticism, we rejected the Hudis-Lidsky Model as a valid model for the Mach probe. In its place, a 2D simulation, which we developed, calibrates our Mach probe. This simulation is essentially a Monte-Carlo integration of the relative currents that reach the upstream and downstream probes. It treats ions as non-interacting particles, a valid approximation considering that the mean free-path in SSX is 10 cm. Instead of including electrons, it invokes an ad-hoc sheath potential. Being two-dimensional, it is able to capture the fact that ions pick up both incoming and transverse kinetic energy, as shown in figure 6.2. Moreover, it uses the actual Gundestrup geometry of the SSX Mach probe.

The simulation is conceptually simple. An ion starts out in a random spot on a sphere centered about the probe, but far from the probe. Its velocity is chosen out of a Gaussian distribution of particles with a drift (see figure 6.1). The particle is allowed to propagate, generally in a straight line, but subject to the sheath electric field when it gets close enough.

The results of the simulation are presented in figure 6.3.

Admittedly, the Falk model has shortcomings of its own. It does not include a pre-sheath potential, and it was only run with SSX parameters. Recently, a rigorous treatment of Mach probes in unmagnetized plasma has been published [40]. Hutchinson's new "SCEPTIC" code uses a 3D Particle-In-Cell method to calculate the pre-sheath potential for a spherical probe in plasma. The result of his simulation is a calibration constant $k = 1.34$ for a broad range of parameters.

Despite this simulation's rigor and inclusion of pre-sheaths, we calibrate the flow data in this thesis with the Falk model, since the geometry of the latter has the "gundestrup" geometry of our probe. The constant k is likely to be at least as dependent on the shape of the probe as whether pre-sheaths are included. We are heartened by the fact that our calibration constant $k = 2.34$ falls in between the Hudis-Lidsky constant $k = 2\sqrt{2}$ and the Hutchinson constant $k = 1.34$. A comparison of the various Mach models is shown in (figure 6.4).

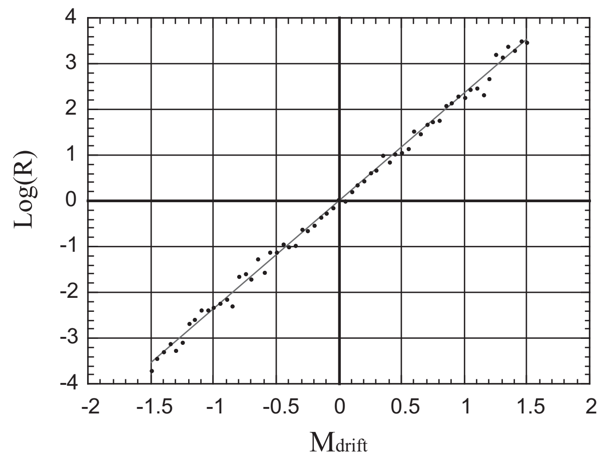

Figure 6.3: The results of the Falk model for the Mach probe calibration. The slope of this graph yields the calibration constant $k = 2.34$.

Model	Type of plasma	Geometry	k (T_i=T_e)	Notes
Hutchinson SCEPTIC	unmagnetized	spherical	1.34	rigorous
Falk Model	unmagnetized	gundestrup	2.34	no pre-sheath
Hudis and Lidsky	unmagnetized	~	2.83	faulty
Integrated Gaussian	unmagnetized	~	3.54	no potentials
Hutchinson	magnetized	~	1.64	fluid model
Chung and Hutchinson	magnetized	~	1.7	kinetic model

Figure 6.4: A comparison of various Mach probe models. The calibration factor k is used to calibrate the Mach probe using the equation $R = \exp(kM)$, where k is the ratio of currents in the upstream to downstream probes and M is the Mach number. References for the table are [40], [30], and [35]

6.5 Mach probe Design

Essentially three Mach probes on one stalk, the "gundestrup" design [36] of the SSX Mach probe allows for measurements of ion flow in an entire plane. There are seven tungsten rods exposed to the plasma: three pairs of opposite Langmuir probes and a center "pride" pin about which the six Langmuir probes (i.e. three Mach probes) are biased. The probes are normally biased negatively with respect to the pride pin so that they will collect ions.

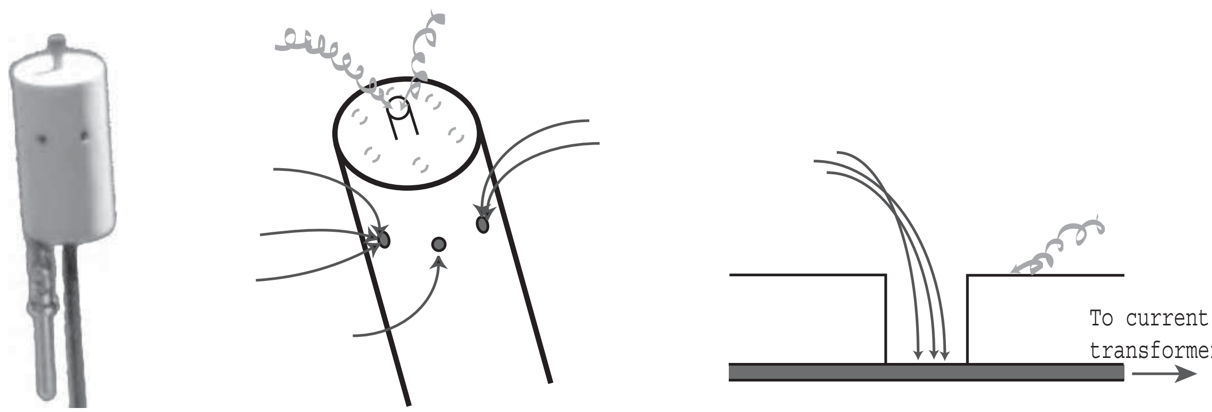

Figure 6.5: The gundestrup probe. The ion gyro-radii are roughly to scale. The electron orbits are really much smaller than the one drawn.

All seven tungsten rods are housed in a boron nitride turret, which is 0.25" in diameter. Carrying the triple blessings of high temperature resistance, low vacuum outgassing, and machinability, boron nitride is a good material for a protective turret. Choosing the area of plasma to which the six ion collecting probes should be exposed is a delicate task, as the twin demons of arcs and low signal delimit a narrow space for this parameter. Our Langmuir probes are exposed to 0.020" diameter circles of plasma. The tungsten probes themselves are a slightly larger 0.025", so that we could know for certain that each hole leads to a full circle of tungsten. The "pride" pin, which receives electrons, is a generous 1 mm in diameter, as this pin should not limit the current on any of the six circuits of the probe. It extends 1 mm from the boron nitride turret.

The current picked up by (any of) the Langmuir probes on the Mach probe should be about $I = nev_tA$. The SSX Mach probe collects currents that peak at 0.1 A. A prototype Mach probe on loan to SSX from Princeton Plasma Physics Laboratory (PPPL) measured currents in SSX that peaked at about 10 A (see figure 7.11). Since the PPPL probe collection area is 8 times the size of the SSX probe, it is currently unclear why the SSX Mach probe collects smaller currents by a factor of 100 instead of by a factor of 8. One possible explanation is that, since the tungsten rods are burrowed more deeply (see figure 6.5c) in the SSX probe than in the Princeton Probe, ions are failing to navigate their way through the "tunnel" to the probe, especially if **B** fields are curving their trajectories.

6.5.1 Connections

A photo of the connections to the Mach probe is shown in figure 6.6. The boron nitride turret has a small lip, so that it can sit atop a 0.25 ” (outer-diameter) non magnetic stainless steel tube. This steel tube contains the electrical connections to the Mach probe and provides the mechanical support for the Mach probe. Since one cannot solder to tungsten, a gold pin crimps to each of the seven tungsten rods. To conserve space in the steel tube, the outside diameter of the gold pins are shaved, the inside diameter of the steel tube is enlarged in the region containing the gold pins, and the gold pins are staggered. The gold pins are coated with heat-shrink to electrically insulate them from each other and the steel tube, and their back ends are soltered to 28-gauge magnet wire.

Passing through an O-ring on the vacuum feed-thru, the steel tube is finally vacuum welded to mini-conflat. Thanks to the O-ring, the steel tube can be raised and lowered to any position along its axis in SSX without removing the probe. The mag wire is soldered to alumina feed-thru pins on this mini-conflat. On the other end of the feed-thru lies a box which receives BNC cables and takes the electrical connections to the screening room, where they meet the biasing circuit.

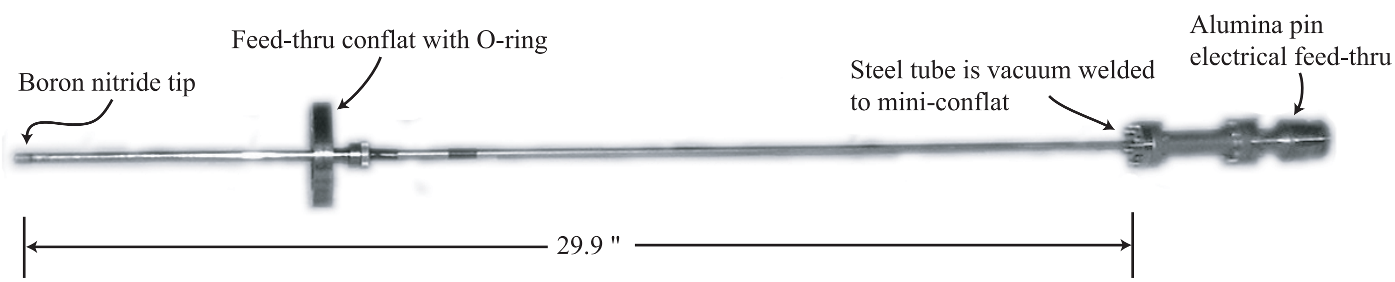

Figure 6.6: The Mach probe in its entirety. The 29.9” length of the Mach probe is measured from the drilled holes in the boron nitride tip to the machine-end of the mini-conflat. The steel tube is vacuum welded to a mini conflat, which is bolted to a connector piece, which is in turn bolted to the electrical feed-thru. The purpose of the connector piece is to make room for the alumina pins on the electrical feed-thru, to which the mag wire is soldered.

6.5.2 Biasing Circuit

The biasing circuit is shown in figure 6.7. A capacitor bank biases each of the six Langmuir probes to -60 V with respect to the pride pin. The capacitors are 88 μF, and each Langmuir probe is biased by two capacitors in parallel (which make one 176 μF capacitor). A 10Ω current limiting resistor is also in the circuit, so that the occasional arc will not damage the electronics. In the time scale of an SSX shot, a few hundred microseconds, the capacitors are essentially a DC power supply. However, it is important to use the capacitor bank instead of power supplies in order to preclude ground loops. Although attached to a charging circuit, once the capacitors are charged, three DPST switches and one SPST switch isolate them from everything but the Mach probe.

Current transformers (Pearson Model 411) measure the current in each of the six probe circuits. Their output is 0.1 V/A, to within an accuracy better than 1%.

Figure 6.7: *Left:* The Mach probe biasing circuit. Before each SSX shot, the six capacitors are charged to 60 V and then isolated. *Right:* The Mach probe Capacitor Bank. Six pairs of capacitors bias the Mach probe. During an SSX shot, the capacitors are isolated from the laboratory, which precludes ground loops on behalf of the Mach probe.

Chapter 7

Results and Discussion

7.1 SXR results

The SXR detector has proven to be a nice detector for SSX. All four filtered-diodes show a signal. Figure 7.1 shows the raw signals of three of these diodes (the fourth, the Indium-filtered diode, has too small of a signal to be seen on this graph). The SXR signals are averaged in bundles of 1 μs to rid the signal of noise. Figure 7.2 is a sample SXR trace with the noise averaged out. Though some be small, the signals from all four filtered diodes are nonzero.

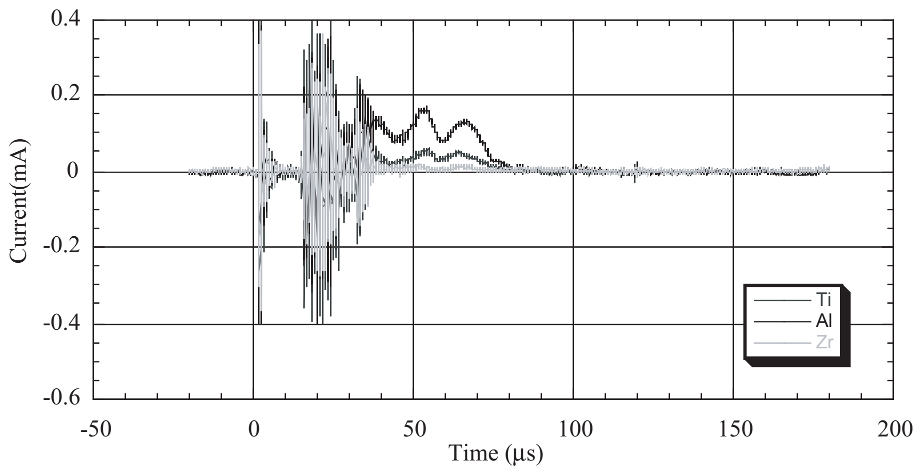

Figure 7.1: The raw SXR signals of three of the diodes. The Indium-filtered diode signal is left out of this figure, as its signal is too small to be seen here.

Figure 7.3 is an interesting sequence of three consecutive shots. These shots happened right after SSX was vented and then re-sealed, so there are still lots of impurities in the vacuum. These impurities impede heating and activity in the plasma, causing the initial SXR signals to be smaller than usual. As the plasma shots clean the vacuum vessel, the SXR signals

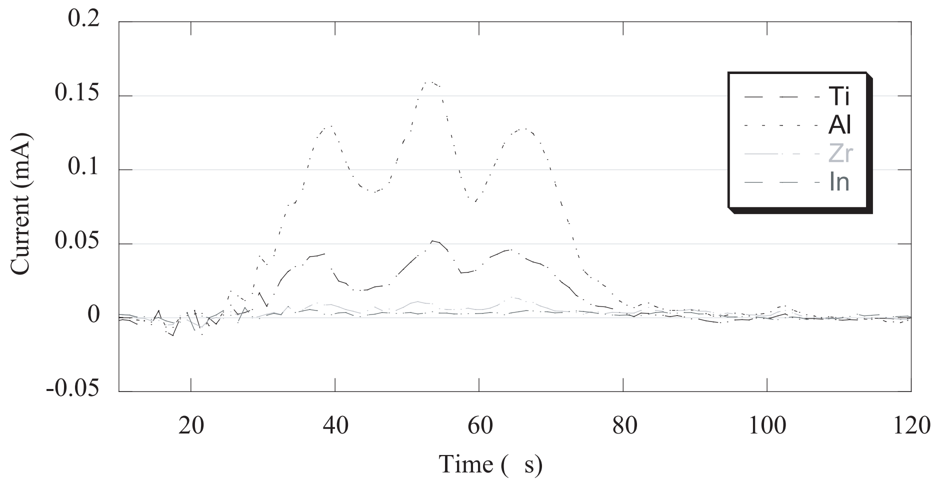

Figure 7.2: A sample signal from the SXR detector. For the magnetic energy corresponding to this signal, see figure 7.4.

rise. As the plasma gets cleaner, though the SXR signals rise, the density is actually gets smaller. This is because among the impurities in the dirty plasma is residual H_2, which is attached to the vessel walls, and which is released when the plasma strikes the walls.

7.1.1 Comparison of SXR signals to magnetic data

The analysis of the SSX-FRC magnetic data is presented in [44] and is a rich topic on its own. Here we would like to discuss the most visible correlations between the SXR signal and the magnetic structure of the FRC. As discussed in chapter 2, it is possible to separate magnetic flux (or magnetic energy) in an FRC in two ways: 1) toroidal vs. poloidal fields, and 2) by the index m of the FRC solution. With the magnetic probes in SSX, we can observe whether a field is $m = 0$ (symmetric mode) or $m = 1$ (tilted mode). Figure 7.4 is a plot of the magnetic energy separated into these four categories.

The reconnection is manifest in the poloidal m=0 magnetic energy plot (lower left). Here, the midplane magnetic energy lags behind the peripheral magnetic energy, which the magnetic flux in the midplane is being consumed by reconnection. As the two poloidal fields reconnect, an FRC is formed. This takes place from plasma ionization (20 μs to 40 μs). If we take the difference between the midplane and peripheral magnetic fields to be a measure of reconnection, the peak reconnection occurs at 35 μs. Meanwhile, the FRC starts to roll over from the $m = 0$ to the $m = 1$ mode, even as the fields are reconnecting. The tilt begins at 45 μs and, by 60 μs, the FRC is maximally tilted.

Since figure 7.4 is from the same shot as the SXR data in figure 7.2, we can directly compare features. The SXR signals have three main peaks: at 38 μs, 53 μs, and 65 μs. The first peak, at 38 μs corresponds to time at which the poloidal reconnection peaks ($\approx$ 35 μs). The second SXR peak, at 53 μs, corresponds to the very center of the developing tilt. This makes sense, since the tilted FRC mode $m = 1$ is a lower energy state than the $m = 0$ mode,

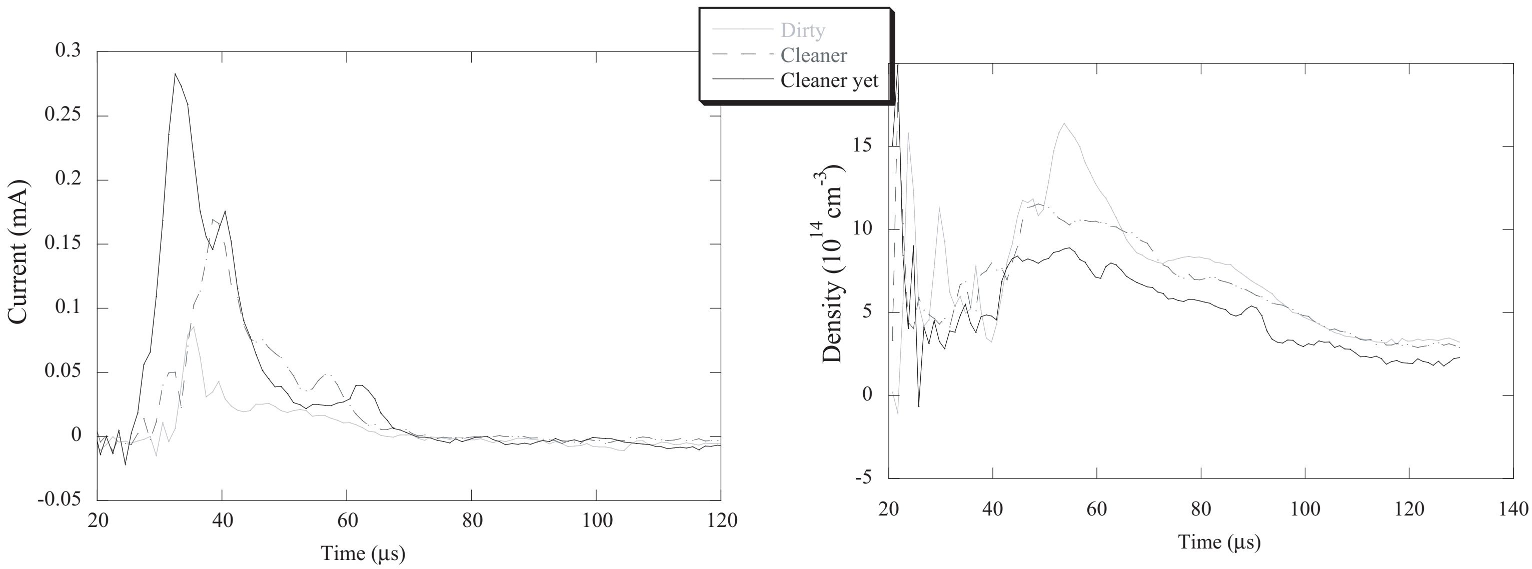

Figure 7.3: A sequence of three consecutive shots in SSX, the first when SSX is at its dirtiest from having been opened. The SXR signal shown is from the Aluminum-filtered diode. The SXR signals rise, while the density falls.

so energy will naturally be released from the plasma as the FRC tilts. It is not so clear what causes the third SXR peak (at 65 μs). It seems to correspond to a local minimum on the $m = 0$ toroidal magnetic energy plot.

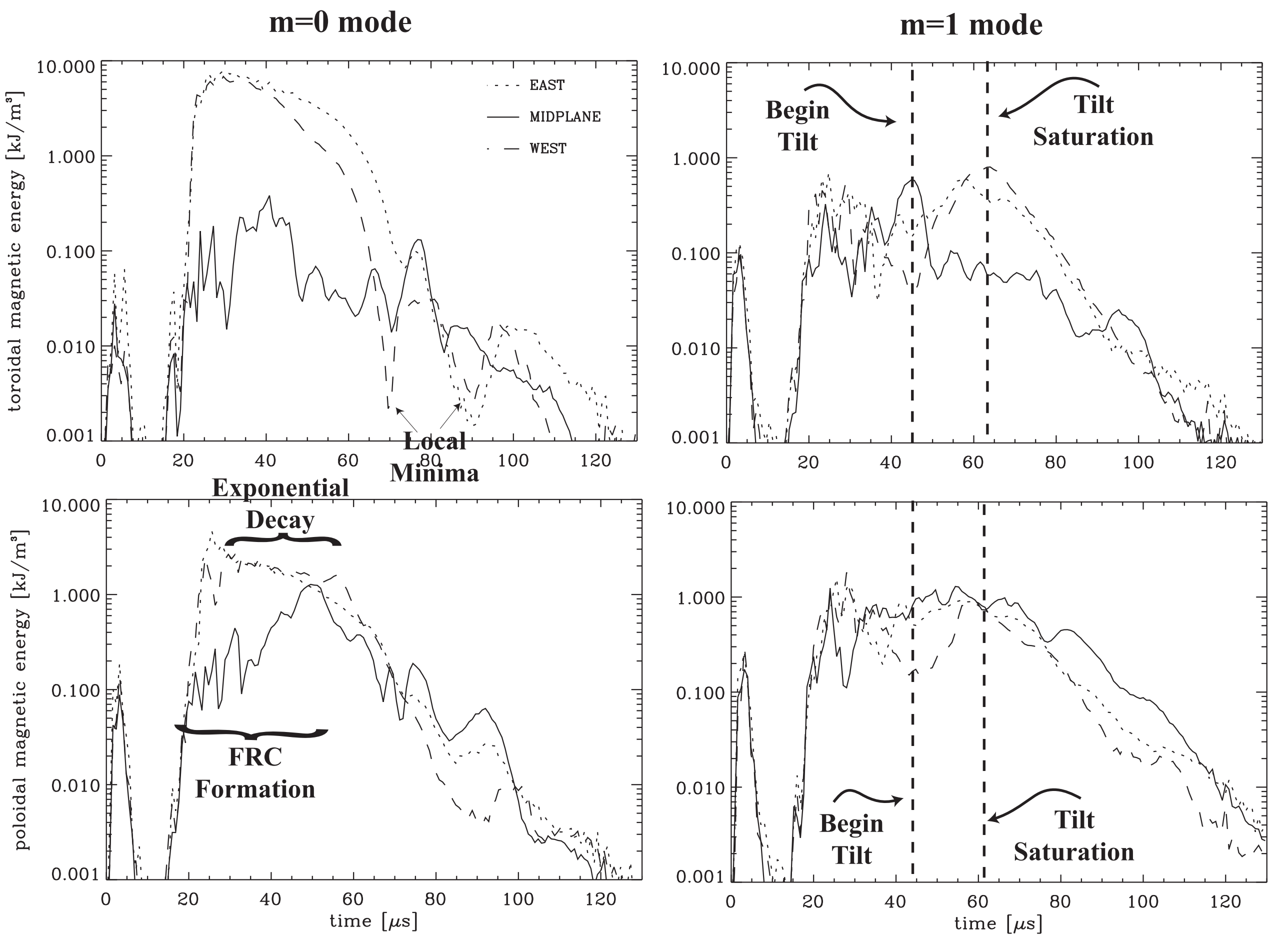

Figure 7.4: A plot of the magnetic energy in SSX, separated into four categories. The shot displayed here is the same shot as the SXR data in figure 7.2.

7.1.2 Temperature-Fitting Analysis and Discussion

The temperature-fitting analysis is a qualified success. A plot of the fitted temperature is shown in figure 7.6, using four different emission spectra as hypotheses. The analysis produces very consistent temperature plots for similar shots in SSX. Each curve in figure 7.6 is really the average of fitted temperatures for 2 different shots. As figure 7.6 makes manifest, the time-dependence of the calculated temperature varies a great deal depending on what impurity hypothesis is used in the calculation. The calculation based on the Spect3D 0% impurity content differs from the pure bremsstrahlung calculation, because the former includes recombination lines and continuum as well as the bremsstrahlung in the emission spectrum. N. B: although we have not been careful to distinguish electron from ion temperature, *the fitted-temperature is really electron temperature*, since electrons are the principal radiators in plasma.

Figure 7.5 is another interesting result of the temperature-fitting analysis. Normally, SSX merges two counter-helicity spheromaks, so that there are fully-opposing magnetic fields at the midplane, which reconnect and form an FRC or a hybrid FRC. However, SSX can also be run in co-helicity mode, where the spheromaks have the same helicity. Instead of forming an FRC when they merge, in this mode they merge into one larger spheromak. As figure 7.5 shows, the stronger reconnection in the counter-helicity mode heats the plasma more than the weaker co-helicity reconnection. Furthermore, the time scale of the more stable FRC is longer than the spheromak. The fitted temperatures are higher in figure 7.5 than in 7.6, because SSX was in a slightly different configuration when figure 7.5 was made, and the plasma was hotter then. The emission model used to calculate the temperature in figure 7.5 is the pure bremsstrahlung model.

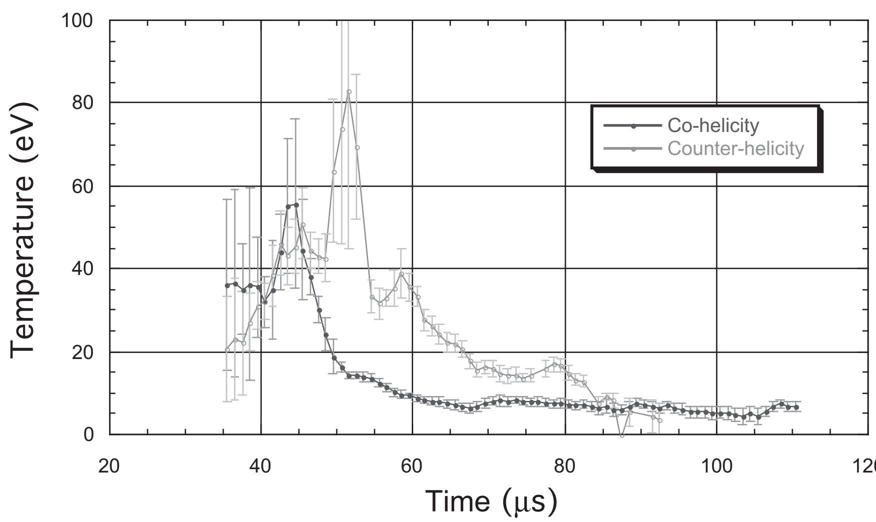

Figure 7.5: A comparison of the temperature in SSX during co-helicity and counter-helicty modes. In the counter-helicity mode, the plasma gets hotter and the time-scale is longer.

A complication of including impurities in the emission spectrum is that, unlike the bremsstrahlung emission spectra which are monotonically increasing functions of temperature (at least for energies greater than 25 eV or so), there is no such monotonicity for the full emission spectra. Figure 7.7 shows this well. Notice that in the impure plasma, the coldest plasma (10 eV) actually emits the most light for most of the 20 eV to 40 eV interval. After 40 eV, the second coldest plasma (20 eV) emits the most light.

This lack of monotonicity explains why the temperature results in figure 7.6 depend not only quantitatively but also qualitatively on the impurity model that is used. At the beginning and the end of an SSX shot, when the SXR signals are small, the bremsstrahlung and Spect3D 0% analyses take the small signals as evidence of low temperatures, whereas the Spect3D 0.5% and 2% analyses take them as evidence of high temperatures. As explained in chapter 5.2, we do not have an *a priori* way of determining the absolute impurity content in SSX (although 2% impurities is definitely on the high end of the possibilities), so there is not a definite way to choose among the temperature plots. At the very least, we can conclude from the way the 0.5% and 2% impurity *ansatzen* result in manifestly unphysical 100 eV plasmas when the plasma is decaying (see figure 7.6) that the impurity content of SSX is likely lower than these numbers.

As figure 7.6 also shows, despite qualitative differences in the dynamic temperature trace, the mean temperature in SSX is roughly consistent, no matter which impurity content we use in the analysis. We find this value to be 30 eV $\pm$ 10 eV. Previously performed VUV spectroscopy has found the temperature of SSX (in a slightly different configuration) to be in the interval 10 eV to 30 eV [43].

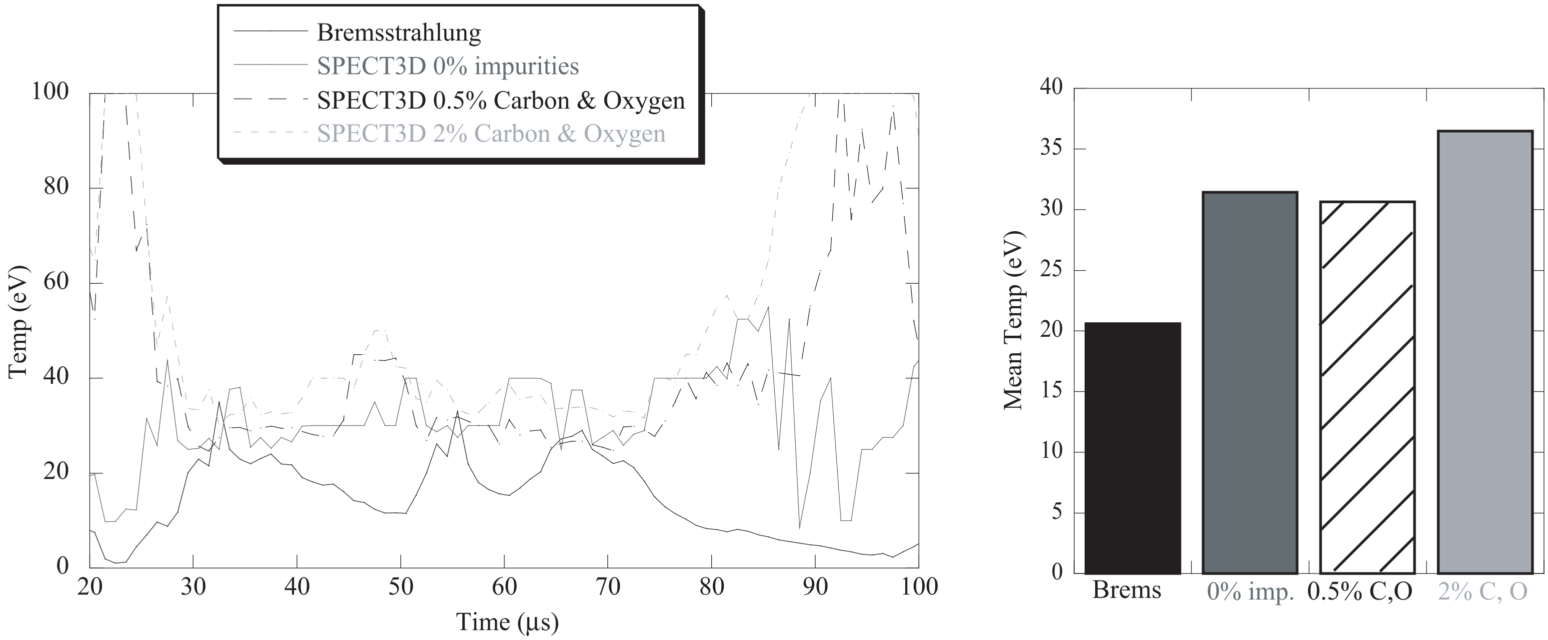

Figure 7.6: *Left:* The temperature of SSX as a function of time, as calculated from the SXR signals and the simulated emission spectrum. The various impurity models yield differing traces. *Right:* The mean temperature from 30 to 70 μs is roughly consistent among the four different emission spectra.

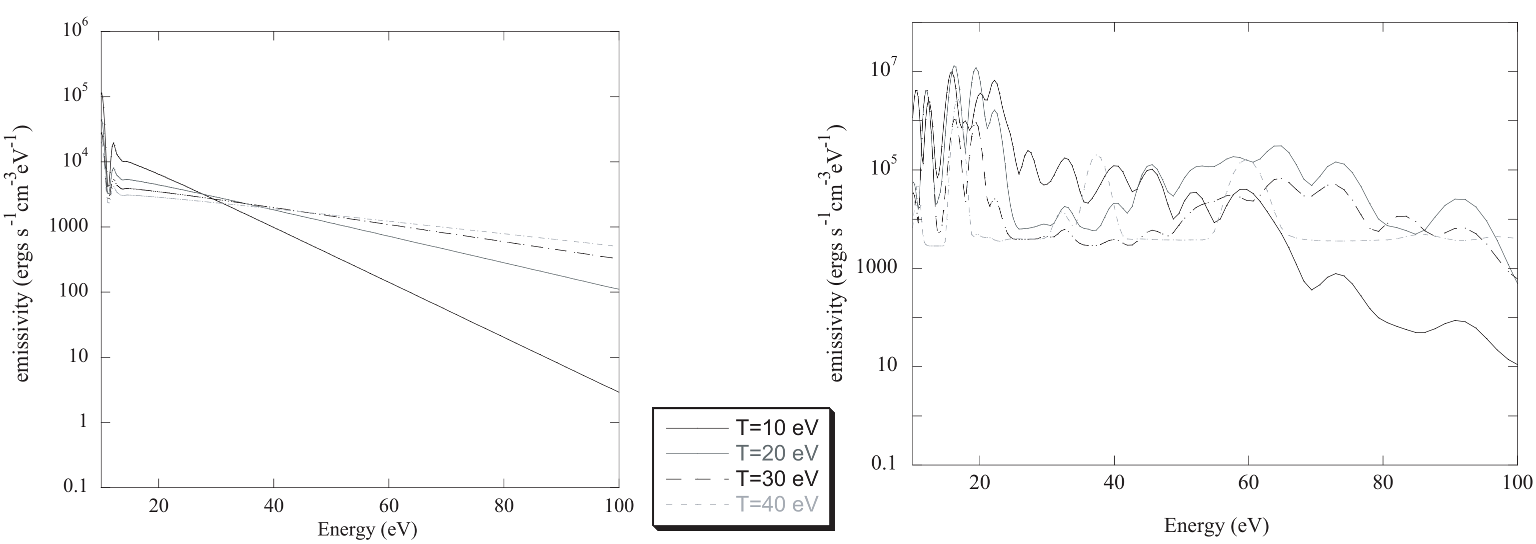

Figure 7.7: *Left:* The emission spectra, as calculated by SPECT 3D, for a pure hydrogen plasma. *Right:* The emission spectra for a plasma with 0.5 % carbon and oxygen (each, by molarity).

7.2 Flow Results

In its current configuration, the SSX Mach Probe can measure ion flow in the $\hat{\theta} - \hat{z}$ plane but not radial flow. The timescale of an SSX shot is shown in figure 7.4. The basic bounds are that plasma is ionized at $t = 20\mu$s and the magnetic structures have more-or-less decayed by $t = 80$ to 100μs. Thus we are looking for flow in the (20,100) μs interval. In the data presented here, the Mach probe is in the midplane of SSX.

Diagnostics like the Mach probe that are in electrical contact with the plasma are notoriously trying partners in science. Like a seaman trying to sail through a stormy shark-filled sea, these diagnostics must frequently navigate through arcing, small signal-to-noise ratios, and damage from the plasma. Indeed, our Mach probe was beset by the first two of these plasma-monsters. Thanks to the stalwart boron-nitride turret, the plasma did not damage the probe, though the probe does show evidence of intense plasma-to-probe contact (see figure 7.8).

Figure 7.8: The Mach probe after a few hundred shots in SSX. Evidence of interaction with plasma on the probe includes 1) shininess on the tungsten due to plasma "cleaning", 2) blackness on the boron nitride due to arcing to impurities, and 3) both blackness and shininess on the steel shaft.

Because of the current transformer's orientation, Mach probe signals are negative. This is arbitrary and signifies nothing. Figure 7.9 shows the unprocessed current through one of the probes in a typical shot. It is hard to see much signal! One thing to notice is that there is a relatively low-frequency ($\approx$ 2-3 μs period) oscillation throughout the signal. It is likely that this oscillation is an actual plasma phenomenon (as oppose to instrumentation noise), as no other SSX diagnostics experience such low-frequency noise.

To partially cleanse the data of this noise, the Mach probe signals are averaged in 5 μs bundles. The cleansed signals from a shot are shown in figure 7.10. The data after 60 μs does not appear to be as trustworthy as the 30-60 μs data. As a comparison, data from the Princeton Mach probe in SSX (which only measures one-component of flow) is shown in figure 7.11. Although signals from the Princeton probe are larger than those from the SSX probe, there are a few ways in which the SSX probe is a better diagnostic. Not only does it measure a plane of flow instead of a single component, but it has less residual glue and, since the thru-holes on the turret are small, the collected current is more acutely directed.

As explained in chapter 6, a non-unity ratio of upstream-to-downstream currents indicates ion flow. The important question now is how can we decide if a current discrepancy in a probe pair is due to real ion flow or whether it is due to some instrumental imprecision (e.g. machining error, mismatched resistors). Happily, there is a good test. If we rotate the

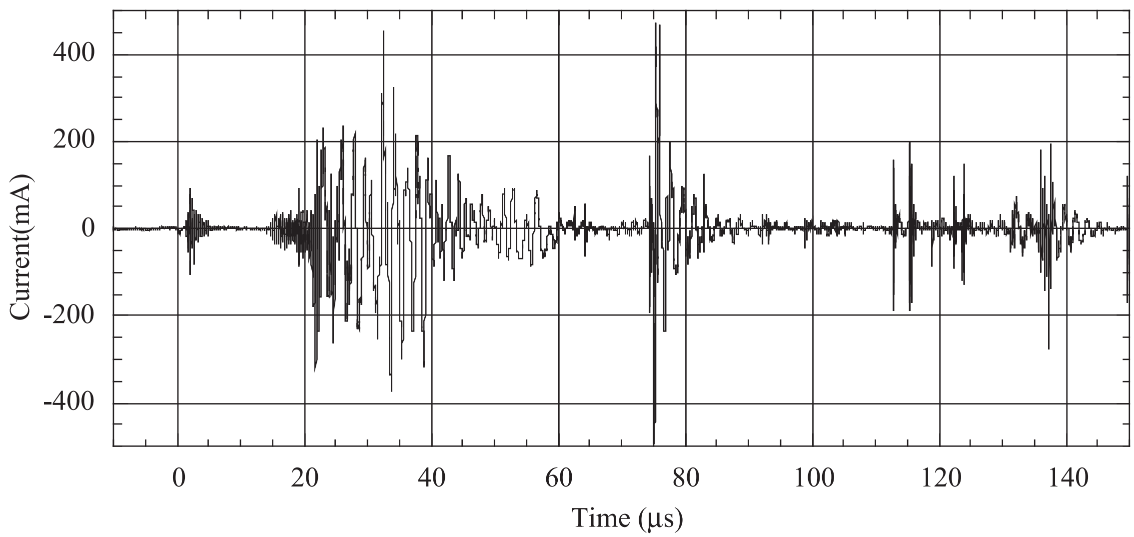

Figure 7.9: A typical trace of the signal through one of the Langmuir probes that compose the Mach probe. Not much signal to see here, although a careful look shows a little bit of (negative) signal around 50 μs.

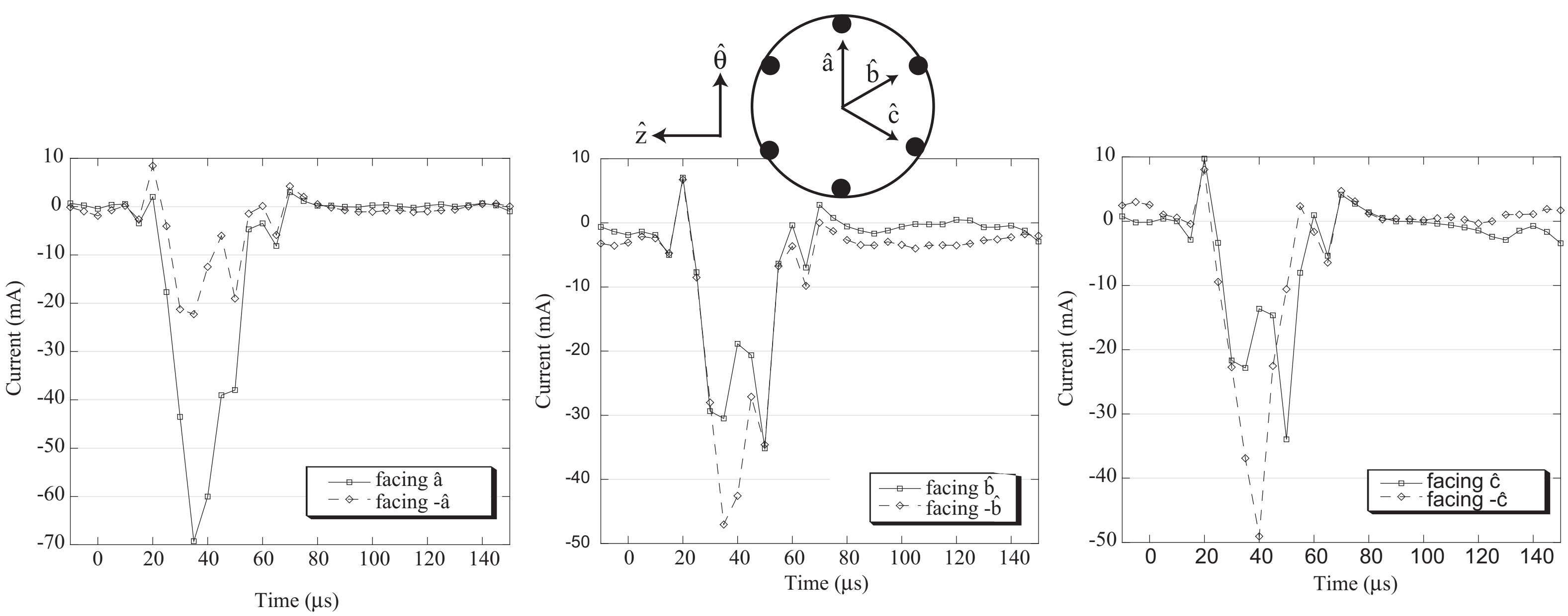

Figure 7.10: The Mach signals, after the noise has been averaged away (as much as possible).

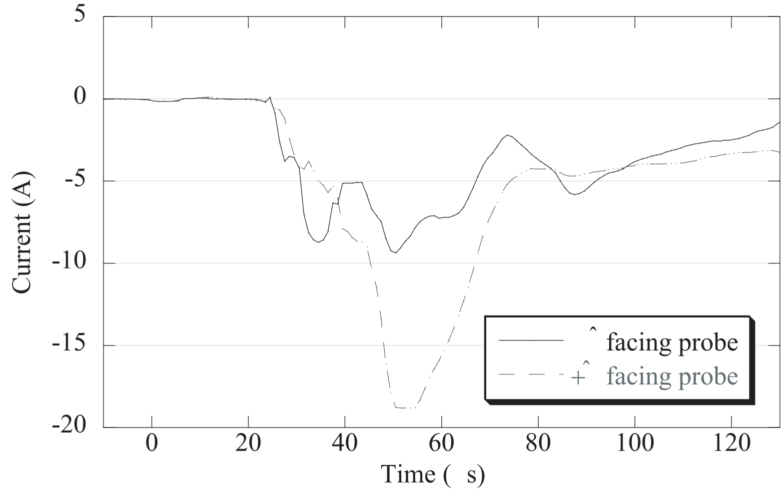

Figure 7.11: A (cleaned) trace from the Princeton Mach probe on loan to SSX.

probe 180 in the plasma, the calculated drift velocity should be opposite. In reality, every shot is different, so we do not exactly see this.

The main result that we observed with the Mach probe is flow in the $+\hat{\theta}$ direction in the 30 to 50 μs interval. Figure 7.12 displays this result, which is seen both with the Princeton Mach probe and the SSX Mach probe. The flow results in figure 7.12 for the Princeton probe is an average of 2 shots for each probe direction, and the flow results from the SSX probe comes from averaging 20 shots. The Mach probe data are calibrated using the Falk Mach model (see chapter 6.4). Note that the only effect of using a different Mach probe model is that the flow result will be scaled by a positive constant, namely the constant k (see figure 6.4). Hence positive azimuthal flow is positive azimuthal flow, no matter what model we use.

The SSX probe also seems to measure a flipping of the azimuthal flow: at $t \approx 75\mu$s, the probe measures flow in the $-\hat{\theta}$ direction. As mentioned above, there is good reason to be mistrustful of the Mach signals at this point. Nevertheless, the Princeton probe also measures flow in the $-\hat{\theta}$ direction around this time. This flow seems to last until about 100 μs, by which time the flow patterns and magnetic structure have largely decayed.

Flow results in the $\hat{z}$ direction are less conclusive. Figure 7.13 summarizes what the Mach probe saw in the two directions that have a $\hat{z}$ component. The $-\hat{c}$-directed flow at 40 μs is likely from the probe picking up a component of the $+\hat{\theta}$ flow.

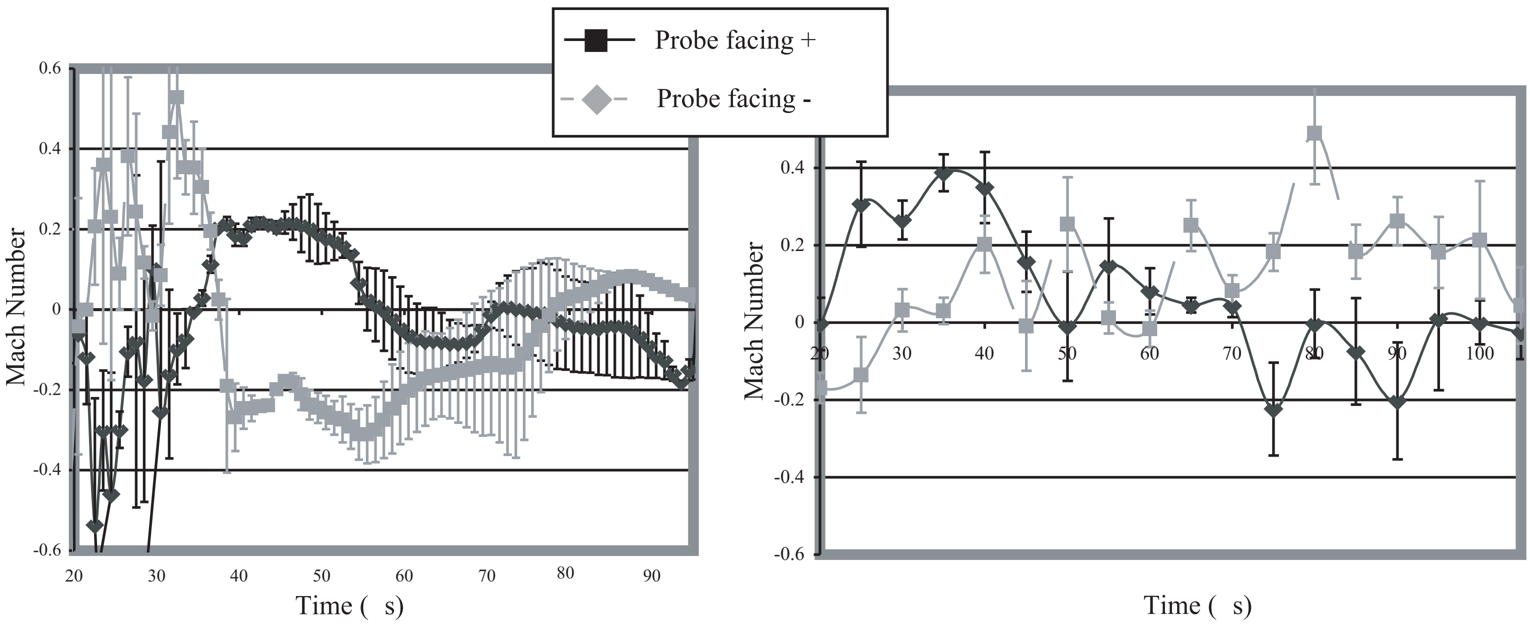

Figure 7.12: The toroidal (azimuthal) flow, as measured by the Princeton Mach probe (*left*) and the SSX Mach probe (*right*). The data are calibrated using the Falk model (see Chapter 6). These flows are averages of the flows on several shots (38 total). If the Mach probe were perfect, and every SSX shot were identical, the grey and black curves would be mirror images.

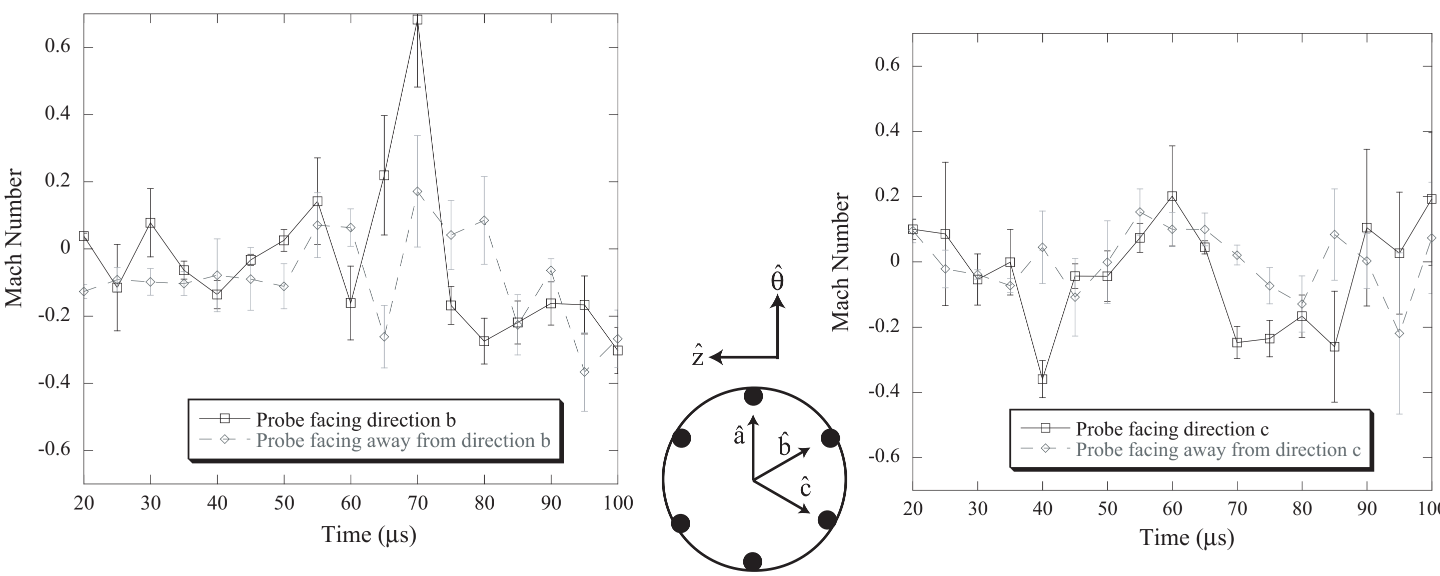

Figure 7.13: Flow measured by the SSX Mach probe in the other two (not purely azimuthal) directions. If the Mach probe were perfect, and every SSX shot identical, the grey and black curves would be mirror images. The probe facing $+\hat{\mathbf{c}}$ measures -$\hat{\mathbf{c}}$ directed flow at 40 μs. These flows are the averages of flows on several shots (8 per line)

7.2.1 Discussion

Toroidal flow has previously been observed [41] in the midplane of a spheromak experiment. In this experiment, they attributed the toroidal flow to $\mathbf{J} \times \mathbf{B}$ forces that operated during spheromak formation, and further noted that this toroidal flow causes a twisting of the poloidal magnetic field into the toroidal direction. This mechanism should be noted as a possible explanation for the anomalously resilient toroidal magnetic fields that SSX measures [44].

The principle $\mathbf{J} \times \mathbf{B}$ flow during spheromak formation is the axial force that pushes the spheromak out of the gun, caused by the $-\hat{\mathbf{r}}$-directed $\mathbf{J}$ toward the center electrode and the toroidal $\mathbf{B}$ from the axial current in the center electrode. However, as the spheromaks form they also "pull" an axial field through the length of SSX. This $\hat{\mathbf{z}}$-directed $\mathbf{B}$, along with the $-\hat{\mathbf{r}}$-directed $\mathbf{J}$ result in a toroidal $\mathbf{J} \times \mathbf{B}$ force. This $\mathbf{J}$ and $\mathbf{B}$ are shown in figure 7.14. The sign of this toroidal force is such that 1) the two spheromaks' $\mathbf{J} \times \mathbf{B} \cdot \hat{\theta}$ add constructively, and 2) the sign is consistent with the direction of flow observed on the SSX Mach probe and the Princeton Mach probe.

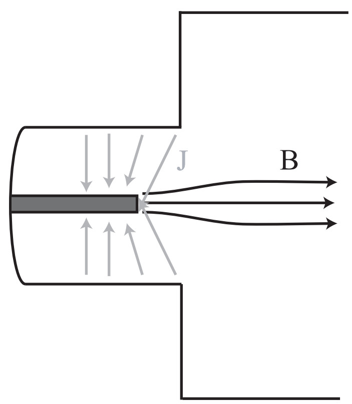

Figure 7.14: A possible mechanism that explains the $+\hat{\theta}$ ion velocity. A $-\hat{\mathbf{r}}$ directed $\mathbf{J}$ and an axial $\mathbf{B}$ give rise to an azimuthal $\mathbf{J} \times \mathbf{B}$.

The Mach probes also measure a reversal of the toroidal flow, starting at about 75 μs, though this flow is more dubious in the $+\hat{\theta}$-flow that is measured earlier. One explanation for this flow is reconnection outflow current, which is discussed in chapter 3.3. Reconnection outflow current is perpendicular to the reconnecting fields so, to explain a toroidal flow, this current would have to be from the reconnecting poloidal fields. On the other hand, reconnection outflow current is not a very satisfactory explanation for toroidal ion flow, since currents in plasma are mostly due to electron, not ion, motion.

7.3 Conclusion

A Succinct Recapitulation of Findings:

1. Two of the three normally-observed SXR peaks are identified. One corresponds to peak reconnection and the other to the peak FRC tilt.

2. From analysis of the SXR signals and emission spectra analysis, the mean (electron) temperature in SSX in the (30 μs, 70 μs) interval is 30 $\pm$ 10 eV. Counter-helicity shots have more peak heating due to more reconnection.

3. Azimuthal (toroidal) flow is observed in the early stages of FRC formation, likely caused by the $\mathbf{J} \times \mathbf{B}$ force during spheromak formation. A possible reversal of this flow is observed as the FRC decays.

The SXR detector and the Mach probe have proven to be good complements to the other SSX diagnostics. Spheromak merging and Field-Reversed Configuration will be continued to be studied in the years to come. Though potentially a magnetic confinement reactor configuration, the FRC's best merit is its illustration of basic plasma principles and its agency in leading scientists to new plasma principles. For plasma physics is still an immature field. In the words of a National Academy of Sciences panel, "Then as now, the obstacles to achieving controlled fusion lay not in our ignorance of nuclear physics, but of plasma physics [5]."

Appendix A

Glossary

β : β is defined to be the ratio of kinetic pressure to magnetic pressure: $\beta = \frac{\mu_0 nkT}{B^2}$

Bremsstrahlung: German for "braking radiation," bremsstrahlung is the radiation given off by charges accelerating as they collide.

Field Reversed Configuration (FRC): An equilibrium genus-1 plasma configuration that has high β. In its ideal form, its magnetic field has no toroidal component, but rather it is entirely poloidal.

Langmuir Probe: The simplest of all plasma diagnostics, the Langmuir probe is essentially a grounded and biased wire that is inserted into the plasma. It can be biased to collect either electrons or ions, and it measures both plasma temperature and density.

Mach Number: The Mach number corresponding to a velocity in a fluid is the ratio of that velocity to the sound speed in the fluid.

Mach probe: A directional *Langmuir probe* used to measure ion flow.

Magnetohydrodynamics (MHD): A simple set of magnetized fluid equations for plasma.

Ohm's Law: The resistive Ohm's law in a plasma is $\mathbf{E} + \mathbf{V} \times \mathbf{B} = \eta \mathbf{J}$.

Poloidal: The direction traced out by circles on a torus that pass "through the donut hole." See *toroidal*.

s: Approximately the number of ion gyroradii in the minor length of a plasma. s is a measure of whether the plasma is fluid-like (high s) or kinetic-like (low s).

Soft x-rays (SXRs): Electromagnetic radiation in the 10 eV to 150 eV range.

Spheromak: An equilibrium low β plasma configuration with both toroidal and poloidal magnetic fields.

SPECT3D: A third-party plasma equilibrium simulation that we use to calculate the emission spectrum in SSX.

SSX (SSX-FRC): The Swarthmore Spheromak Experiment. The 'FRC' (Field-Reversed Configuration) was appended to the name two years ago, but nevertheless, we often refer to the experiment as plain SSX for short.

Toroidal: The azimuthal θ direction in cylindrical geometry. "The long way around the doughnut." See *poloidal*.

Bibliography

[1] F. F. Chen, *Introduction to Plasma Physics and Controlled Fusion*, Plenum Press, New York 1974 (revised 1984)

[2] J. Geoffrey Cordey, Robert J. Goldston and Ronald R. Parker *Progress Toward a Tokamak Fusion Reactor*. Physics Today, January 1992

[3] M. Brown, *Sweet-Parker reconnection: scaling for reconnection rates*, Swarthmore College

[4] Bellan, Paul M., *Spheromaks*, Imperial College Press (2000)

[5] National Research Council, Panel on the Physics of Plasmas and Fluids, Physics Survey Committee, Physics Through the 1990s; Plasmas and Fluids (Washington, DC: National Academy Press, 1986), p. 4.

[6] Y. Ono *et al.*, Phys. Fluids B **5** (1993) 3691

[7] G. B. Rybicki, A. P. Lightman, *Radiative Processes in Astrophysics*, John Wiley & Sons, New York

FRC References

[8] C.D. Cothran, A. Falk, A. Fefferman, M. Landreman, M. R. Brown, M. J. Schaffer, *Partial and Complete Spheromak Merging at SSX: 3D Studies of Reconnection and FRC Formation*, Phys. Plasmas, submitted 11/02

[9] M. J. Schaffer, M. R. Brown, J.A. Leuer, P. B. Parks, C.D. Cothran, *Advances in Novel FRC Plasmas*, General Atomics Project 04437 (2002)

[10] M. Tuszewski, Nucl. Fusion **28**, 2033 (1988)

[11] M. Tuszewski, D. P. Taggart, R. E. Chrien, D. J. Rej, R. E. Siemon, and B. L. Wright, Phys. Fluids B: Plasma Phys. **3**, 2856 (1991)

[12] J. T. Slough and A. L. Hoffman, Nucl. Fusion **28**, 1121 (1988)

[13] E. Belova, S. C. Jardin, H. Ji, M. Yamada, and R. Kulsrud, Phys. Plasmas **7**, 4996 (2000)

[14] Y. A. Omelchenko, M. J. Schaffer, and P. B. Parks, Phys. Plasmas **8**, 4463 (2001)

[15] Y. A. Omelchenko, Phys. Plasmas **7**, 1443 (2000)

[16] Center for New Technology and Energy, Italy, http://www.frascati.enea.it

Soft X-Ray Detector References

[17] F. Hansen, Ph.D. Thesis, Caltech (2001)

[18] I. V. Khutoretsky, Rev. Sci. Instrum., **66**, 774 (1995)

[19] S. Hokin, R. Fonck, P. Martin, Rev. Sci. Instrum. **10**, 5038 (1992)

[20] L.J. Terminello, A. B. McLean, A. Santoni, E. Spiller, F.J. Himpsel, Rev. Sci. Instrum. **61**, 1626 (1990)

[21] V. A. Soukhanovskii, D. Stutman, M. Iovea, M. Finkenthal, H.W. Moos, T. Munsat, B. Jones, D. Hoffman, R. Kaita, R. Majeski, Rev. Sci. Instrum. **72**, 737 (2001)

[22] L. R. Canfield, R. E. Vest, R. Korde, H. Schmidtke, R. Desor, Metrologia, **35**, 329 (1998)

[23] H. Funsten, S. M. Ritzau, R. W. Harper, R. Korde, IEEE Transactions in Nucl. Sci. **48**, 1785 (2001)

[24] http://www-cxro.lbl.gov/optical_constants/filter2.html, X-ray Interactions with Matter, Lawrence Berkeley National Laboratory

[25] X-ray WWW Server, Uppsala University, http://xray.uu.se/hypertext/henke.html

[26] http://www.prism-cs.com/software/spect3d/index.htm

[27] G. C. Idzorek and R. J. Bartlett, *Silicon photodiode characterization from 1 eV to 10 keV*, Los Alamos National Laboratory (2002)

[28] Online Cables. Their website is http://www.onlinecables.com

Mach probe References

[29] I.H. Hutchinson, Physics of Plasmas, **9**, 1832 (2002)

[30] M. Hudis and L. M. Lidsky, J. Appl. Phys. **41**, 5011 (1970)

[31] B. J. Peterson, J. N. Talmadge, D. T. Anderson, F. S. B. Anderson, J. L. Shohet, Rev. Sci. Instrum., **65**, 2599 (1994)

[32] S. C. Hsu, *Experimental Study of Ion Heating and Acceleration During Magnetic Reconnection*, PPPL (2000)

[33] Shinohara S, Matsuoka N and Matsuyama S 2001 *Phys. Plasmas* **8** 1154

[34] P.J. Harbour and G. Proudfoot, J. Nucl. Materials, **121** (1984)

[35] I.H. Hutchinson, Phys. Fluids **30**, 3777 (1986)

[36] C. S. MacLatchy, C. Boucher, D. A. Poirier, J. Gunn, Rev. Sci. Instrum., **63**, 3293 (1992)

[37] J.P. Gunn, C. Boucher, I. Duran, K. Dyabilin, J. Horacek, M. Hron, J. Stockel, G. Van Oost, H. Van Goubergen, F. Zacek, Phys. of Plasmas, **8**, No. 5 (2000)

[38] G. A. Emmert, R. M. Wieland, A. T. Mense, J. N. Davidson, Phys. Fluids **23**, 803 (1980)

[39] N. Hershkowitz, *Plasma Diagnostics: Discharge Parameters and Chemistry* (Academic, New York, 1989)

[40] I. H. Hutchinson, *Plasma Phys. Control. Fusion* **44** (2002)

[41] B. Barrow, G. C. Goldenbaum, Phys. Rev. Let., **64** (1990)

SSX Theses

[42] T. W. Kornac, *Magnetic Reconnection Studies on SSX*, Swarthmore College Honors Thesis (1998)

[43] Lukin, V. S. *Modeling SSX Spheromak Plasmas: Internal Physics from External Measurements*, Swarthmore College Honors Thesis (2000)

[44] A. Fefferman, *Formation and Stability of Spheromak/Field Reversed Configuration (FRC) Hybrids in SSX-FRC*, Swarthmore College Honors Thesis (2003)